## ABSTRACT

Title of Dissertation: A-DEPENDENCE OF PHOTOPRODUCED JETS AND COMPARISON WITH HADROPRODUCTION

Donna Lynne Naples, Doctor of Philosophy, 1993

Dissertation directed by: Chia-cheh Chang, Professor of Physics
Department of Physics

Fermilab experiment E683 studied photoproduction of jets produced with a high energy real photon beam incident on nuclear targets. Data were collected with a segmented large acceptance calorimeter. The photon beam, which ranged in energy from 50-400 GeV, is the highest in existence and allowed us to study jet production which was inaccessible to previous experiments at lower $\sqrt{s}$. Jets with $P_t$ in the range 3-7 GeV were reconstructed.

The event structure of photoproduced jets will be presented in the context of a comparison with our data taken using a broad momentum $\pi^-$ beam at the same mean $\sqrt{s}$. Differences in event $E_t$ flow were seen in the two cases and will be presented. The differences are studied in the context of a Monte Carlo comparison.

Measurements of A-dependence in photoproduced jets are presented for the first time in this thesis. A strong A-dependence is observed in the kinematic variable $K_{t\phi}$, which is the out of plane component of the transverse momentum. A-dependence in longitudinal energy flow will also be discussed. The A-dependences



HAC5210

will be compared with those taken with the pion beam incident on nuclear targets. Because of the wide range of energies provided by the bremsstrahlung beam we were able to measure the behavior of the nuclear contributions to $K_{\ell\phi}$ with $\sqrt{s}$.

# A-Dependence of Photoproduced Jets and Comparison with Hadroproduction

by

Donna Lynne Naples

Dissertation submitted to the Faculty of the Graduate School
of The University of Maryland in partial fufillment
of the requirements for the degree of
Doctor of Philosophy
1993

Advisory Committee:

Professor Chia-cheh Chang
Professor Harry D. Holmgren
Professor Philip G. Roos
Professor Alice C. Mignerey
Associate Professor Thomas D. Cohen

## DEDICATION

To Mom, Dad, David, Colleen, and Amy

who taught me the most important thing.

"Physics isn't the most important thing; love is."

– *Richard P. Feynman*

## ACKNOWLEDGEMENTS

For all of those of you who experienced this phase of my existence with me, taught me, or helped me (even in a way I did not recognize as help at the time) I say sincerely now, "Thank you!". As I grow in experience I realize the value of such help and will strive to repay the favor by helping others in the same way if possible.

Only the best thesis advisor can convey his own excitement and enthusiasm for a field of research to a student and that is why I choose George Chang as my thesis advisor. The biggest thanks goes to him for passing on to me not only his expertise in the fields of QCD and nuclear physics but also his enthusiasm for the subject, both of which I will treasure.

I would also like to say many thanks to Harry Holmgren who has been a co-advisor on this work. Harry has the uncanny ability to ask just the right question and get the the point of matters. Every one of his suggestions have been very useful and always turned out to be precisely the right thing to do.

Marj Corcoran has also helped me greatly. During her two years of residence at Fermilab to work on 683, I have learned so many things from her that there is just no way to be specific. She supervised every aspect of 683 during which time she earned the well deserved title, "our fearless leader". She has not gotten enough thanks and recognition. I would especially like to thank her for her personal

involvement in my thesis research, career, and life.

Peter Kasper (alias E683 scape-kangaroo) is owed many thanks for his critical evaluation of my work. Peter could see a tiny flaw in an arguement from 10 miles away (I think he got that from bird watching). That is to say, without being directly involved in the details of the work he could point out the details of the details which you hadn't even thought of yet (and of course he couldn't wait to point them out). Also, his patience and guidance with the analysis effort at Fermilab was greatly appreciated.

Don's placement in the thank you list in no way reflects his contribution to my thesis and scientific education. He should be in fact be near the very top of the list (but he understands). The statement of fact is that Don Lincoln is one of the best teachers I've ever had. He is the resident expert on everything I don't know or am not sure about. I am truely indebted to him for his patience with me and we are all indepted to him for his many contributions to the success of 683. I would especially like to thank him for explaining to me so clearly many specific things which 7 years of graduate school had not succeeded in getting across.

Many thanks to all the 683 collaborators especially the grad students, John Marraffino, and Med Webster who did the bulk of the shifts, detector testing, and preparation for their many hard hours of work that lead to a sucessful data taking period for E683. I would also like to thank Dave Northacker for his superb job of

designing, building, and operating the 683 gas system and to Roy Justice for his expert technical assistance.

I would also like to thank Mike Longo, Dick Gustafson, and Herbert Breuer for their many helpful suggestions and for the many incidents where their hardware expertise saved the day.

I also appreciate the friendship and encouragement I got from the Nuclear physics group at Maryland especially Nick Chant and Phil Roos.

Thanks to Gavin, Farida, Mohammad and Tao for their friendship and for their patience in waiting for my return from the midwest. For the many good vibes thanks to Steve and G.

Many thanks to Judy Myrick, Janet Anderson, Jane Hessing and Bernie Kozlowski for helping me in many ways with UMD red tape while I was at Fermilab.

A special thanks Super Craig for his 'Craig antics' that kept me and Marj entertained while we lived at Fermilab - and for waking me up every morning.

To my family, to whom I owe everything that I am, thanks for believing in me.

*"Non nobis Domine sed nomine tuo da gloria." - Psalm 115*

# TABLE OF CONTENTS


| Section | | Page |
|---|---|---|
| List of Figures | | ix |
| List of Tables | | xii |
| **1 Physics Perspective** | | 1 |
| 1.1 | Introduction | 1 |
| 1.2 | Hard Interactions of the Photon | 4 |
| 1.3 | Fragmentation and Jet Physics | 9 |
| 1.4 | Nuclear Medium Effects | 13 |
| **2 Description of the Experiment** | | 18 |
| 2.1 | Beamline | 18 |
| 2.1.1 | Photon energy tagging system | 21 |
| 2.2 | E683 detector | 26 |
| 2.2.1 | Overview | 26 |
| 2.2.2 | Main Calorimeter | 26 |

2.2.3 Wire Chambers . . . . . 30

2.2.4 Forward Calorimeter and Pileup Monitor Device . . . . . 35

2.2.5 Targets . . . . . 38

2.3 Triggering . . . . . 39

2.4 GEANT Study of Photon Beamline . . . . . 44

**3 Event Reconstruction and Selection** **50**

3.1 Data Aquisition . . . . . 50

3.2 Data Reduction . . . . . 51

3.3 Event Selection . . . . . 51

3.4 Jetfinding . . . . . 56

**4 Monte Carlo Studies** **64**

4.1 Generators . . . . . 64

4.2 Detector Simulator . . . . . 66

4.3 Monte Carlo Comparison with Data . . . . . 68

4.4 Jetfinding Studies . . . . . 71

4.5 Jetfinding Correction . . . . . 74

**5 Results and Discussion** **77**

5.1 Differences in $\gamma p$ and $\pi p$ Jet Events . . . . . 77

5.2 A-dependence of $K_{t\phi}$ . . . . . 89

5.3 Energy Dependence . . . . . 99

5.4 A-Dependence in Other Variables . . . . . 105

5.5 Conclusions . . . . . 110

Appendix . . . . . 113

Bibliography . . . . . 114

# LIST OF FIGURES


| Number | | Page |
|---|---|---|
| 1 | Direct coupling processes in photoproduction . . . . . | 6 |
| 2 | Extended photon processes in photoproduction . . . . . | 7 |
| 3 | Cross section predictions from pQCD . . . . . | 8 |
| 4 | Wideband tagged photon beamline . . . . . | 19 |
| 5 | Incident electron beam momentum spectrum . . . . . | 22 |
| 6 | Photon energy spectrum and RESH bin population . . . . . | 25 |
| 7 | E683 detector (top view) . . . . . | 27 |
| 8 | MCAL closeup . . . . . | 28 |
| 9 | TDC spectrum for typical drift plane wire . . . . . | 33 |
| 10 | Pile up monitor readouts . . . . . | 38 |
| 11 | Simulated photon spectrum at E683 target . . . . . | 49 |
| 12 | Fraction of photon energy remaining at E683 target . . . . . | 49 |
| 13 | Triggered $E_t$ spectrum . . . . . | 54 |

14 Event planarity of the triggered data sample . . . . . 56

15 Average jet $P_t$ spectrum . . . . . 59

16 E683 Coordinate System . . . . . 61

17 Planarity of di-jet event sample . . . . . 62

18 Kinematic correlations of the di-jets events . . . . . 63

19 Comparison of jet events with Monte Carlo . . . . . 69

20 $E_t$ flow comparison with Monte Carlo . . . . . 70

21 Jetfinding studies in $P_t$ and $\phi$ . . . . . 73

22 Flow diagram for jetfinding correction . . . . . 75

23 Pion beam momentum spectrum . . . . . 78

24 Average jet $P_t$ dependence of planarity . . . . . 79

25 $\Delta\phi$ spectrum for $\gamma p$ and $\pi p$ . . . . . 81

26 Expected contributions to $\Delta\phi$ . . . . . 83

27 $K_{t\phi}$ vs $P_t$ for $\gamma p$ and $\pi p$ Monte Carlo comparison . . . . . 85

28 Underlying event comparison $\pi p$ and $\gamma p$ data . . . . . 88

29 HERWIG comparison with TWISTER $\pi p$ underlying event . . . . 88

30 Uncorrected A-dependence of $K_{t\phi}$ . . . . . 90

31 A-dependence of $\Delta\phi$ . . . . . 91

32 Effect of empty target correction on A-dependence . . . . . 93

33 A-dependence of $K_{t\phi}$ after empty target correction . . . . . 94

34 Nuclear contribution to $K_{t\phi}$ . . . . . 95

35 $K_{t\phi}$ measured for each target . . . . . 98

36 Non-jet $E_t$ fraction for each target . . . . . 100

37 A-dependence of $K_{t\phi}$ at different photon beam energies . . . . . 101

38 Nuclear contribution to $K_{t\phi}$ for ranges of beam energies . . . . . 103

39 Energy dependence of $k_{t\phi NUCLEAR}$ vs A . . . . . 104

40 A-dependence of forward energy flow . . . . . 106

41 A-dependence of energy flow . . . . . 107

42 A-dependence of event planarity . . . . . 109

# LIST OF TABLES


| Number | | Page |
|---|---|---|
| 2.1 | RESH tag bin energies | 24 |
| 2.2 | Time to distance fits for Monster drift chambers | 34 |
| 2.3 | E683 targets | 40 |
| 2.4 | Beamline material included in GEANT simulation | 47 |
| 2.5 | Summary of photon beam losses results | 48 |
| 4.1 | Monte Carlo event generators studied. | 66 |
| 5.1 | Fitted offsets of energy dependence curves | 102 |

# Chapter 1

# Physics Perspective

## 1.1 Introduction

The understanding of nuclear matter and phenomena have gradually evolved leading us from the study of nuclear structure and nucleon interactions into the study of nucleon substructure and parton interactions. This evolution was precipitated by the observations of evidence for nucleon substructure obtained at SLAC in the late 60's[1] and the concurrent development of the quark model[2]. The quark model was very sucessful in explaining hadron spectroscopy. While quarks were the prime candidate for the sub-nucleon constituent directly convincing evidence could not be found for this favored interpretation. It was only after much experimental work, the development of QCD, and the realization of jets that the

association could convincingly be made.

The study of large transverse momentum phenomena played a major role in this development. In 1972, the first measurements of single particle cross sections in the high transverse momentum regime resulting from p-p collisions at $\sqrt{s}$ up to 62.4 GeV yielded suprising results for the $P_t$ dependence of the cross section. The measurements yielded a behavior of $P_t^{-8}$ [3] while predictions based on Rutherford scattering of point constituents predicted a drastically different dependence of $P_t^{-4}$. This along with the inability to specify the quantum numbers of the partons prevented their association with quarks. It was only when this experimentally confirmed $P_t$ dependence was understood in the context of the theory of QCD[4] that an understanding of the nature of the nucleon constituents and interactions was finally achieved.

The theory of Quantum Chromodynamics (QCD) defines a theory of strong interactions. QCD is a field theory in which quarks interact with each other via exchange of field quanta called gluons. The quantum number that the field is sensitive to is called color. The color quantum number has three values; red, green, or blue. This is in contrast to the theory of electromagnetic interactions, QED, in which there is a single valued quantum number, electric charge. Another very important difference is that in QCD the field is 'non-Abelian'. This allows for the field quanta themselves to have color charge. Because of this property the

gluons can interact with each other. Recently, the non-Abelian nature of QCD has been experimentally confirmed through the observation of the triple gluon vertex[5].

The non-Abelian structure of QCD makes it much harder to study than QED. The consequences of gluon self interaction lead to a potential energy that increases linearly with the seperation of the color charges. Thus an infinite amount of energy must be supplied to seperate two color charges to infinity. This property is refered to as color confinement and is believed to be responsible for the unobservability of free quarks in nature. At short range, the color screening effect of gluon self interaction leads to a reduced field strength. The color charges are said to be 'asymptotically free'. The strong interaction is thus described by a running coupling constant, $\alpha_s(Q^2)$, given to first order by:

$$\alpha_s(Q^2) = \frac{12\pi}{(33 - 2n_f)\log(Q^2/\Lambda^2)}$$

Where $\Lambda$ is an arbitrary parameter introduced by renormalization. It is determined from experiment to be on the order of 200 Mev ($\pm$ 100 MeV). $Q^2$ is the squared four momentum transfer by the field quanta which characterizes the length scale of the interaction and $n_f$ is the number of quark flavors of the theory. Additional terms are needed if $Q^2$ becomes sufficiently small.

In QCD, perturbation theory can only be applied at high $Q^2$ (short distances) where the coupling strength is sufficiently small (i.e. for $Q^2 \gtrsim (30\ \text{GeV})^2$). So

far, many aspects of the theory of QCD have been tested especially in the regime where perturbative expansions can be used to simplify the predictions. This is called pQCD, for perturbative QCD. Perturbative expansion techniques are not applicable at low $Q^2$. The low $Q^2$ region is at present largely unexplored and is lacking in theoretical predictions [6]. Included in this realm are the nucleon-nucleon interactions which are understood only qualitatively from the theory of QCD.

This chapter will discuss the nature of the hard processes involved in photoproduction, the complications to measurement due to fragmentation, and discuss progress in understanding of QCD from the study of the passage of partons through nuclear matter.

## 1.2 Hard Interactions of the Photon

Large transverse momentum particles can be produced in the collision of hadrons at high enough $\sqrt{s}$ ($\gtrsim$20 GeV). This phenomenon is interpreted as resulting from a hard scattering of the participating hadron constituents. Hard interactions are characterized by the transverse momentum, $P_t$, which they impart to the partons in the scatter. Thus the transverse momentum of the outgoing partons can be used to characterize the momentum transfer scale in the hard scattering, $Q^2$, ($Q^2 \propto P_t^2$).

A more efficient way to produce high $P_t$ interactions is to use a real photon beam. In the collision of a photon with a hadron the photon can transfer all of its energy to the reaction. In hadroproduction the interacting constituent has only a fraction of the total beam momentum. In addition, leading order 'direct' coupling processes in photoproduction are calculable in perturbative QCD and less cumbersome than in the hadron-hadron case. (There are only two processes involved).

Until recently high enough energy photon beams were not available for the study of high $P_t$ production. E683 data was taken at the highest energies so far studied by photoproduction. The photon energies ranged from about $100 < E_\gamma < 400$ GeV which corresponds to maximum parton $P_t$'s of about 10 GeV. Previous photoproduction experiments [7][8] studied single particle inclusive reactions up about 170 GeV in energy.

The lowest order direct coupling (also called pointlike coupling in this thesis) processes are photon-gluon fusion ($\gamma g \rightarrow q\bar{q}$) and QCD compton ($\gamma q \rightarrow gq$). The Feynman diagrams for the processes are shown in figure 1a and 1b respectively. Both processes are $O(\alpha_{em}\alpha_s)$. It should be noted that these processes dominate over purely electromagnetic channels by about two orders of magnitude at these medium range $Q^2$'s ($\alpha_s \sim 0.5$ in our $P_t$ range). These processes each result in two high $P_t$ partons balancing each other in $P_t$ and a remnant di-quark travelling

backward in the center of mass frame.

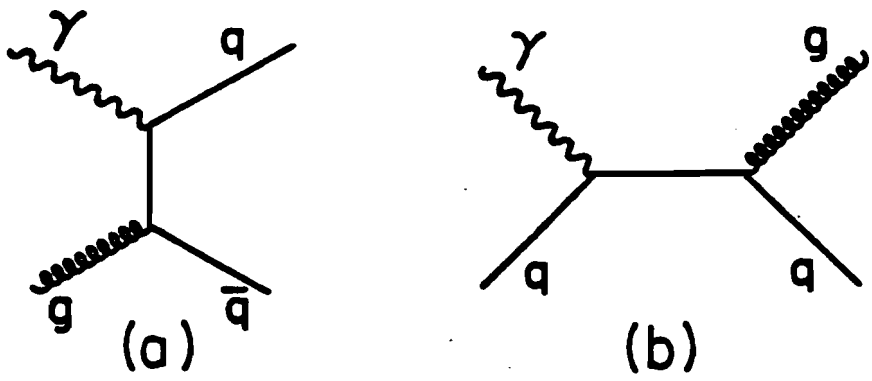


Figure 1: Diagrams for the leading order direct coupling processes in photoproduction a.) $\gamma g$ fusion b.) QCD compton.

A photon can also act as an extended object through its hadronic structure which arises from its direct coupling to quarks. For some fraction of its interactions, the photon can act as a $q\bar{q}$ pair or as a vector meson, ($\rho^o$,$\omega$,$\phi$). Probabilities for these interactions can be described by the photon's structure function. Usually the contributions from the photon structure function are seperated into two parts; the so called 'anomalous' part in which the $q\bar{q}$ pair can be treated in perturbative QCD (i.e., the quark and antiquark are resolved), and the VDM (vector dominance model) part in which the photon interacts as a vector meson. The two types of processes are represented in figure 2. The resolved processes are $O(\alpha_s^2)$, however, and the photon structure function is $O(\alpha_{em}/\alpha_s)$ so the resolved processes are of the same order as the direct processes in $\alpha_s$ [9]. At present the photon structure function is not well determined by experiment. The theoretical

predictions vary substantially (especially for $x \lesssim 0.1$).

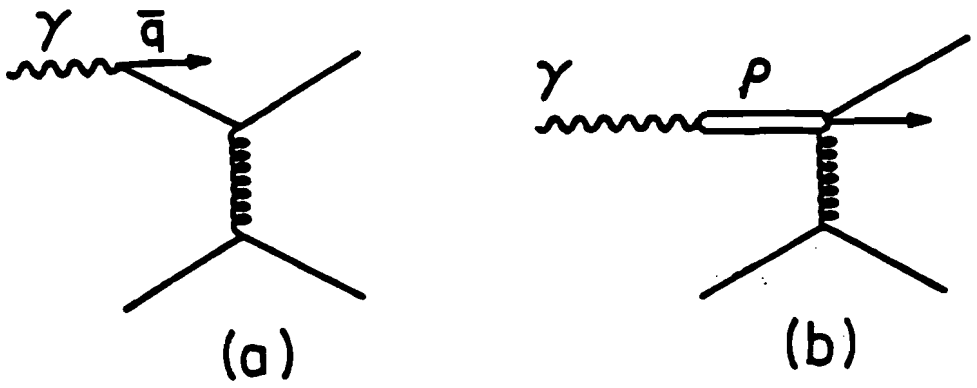


Figure 2: Diagrams for the leading order extended photon processes in photoproduction a.) 'anomalous' processes in which the photon couples to a resolved $q\bar{q}$ pair b.) VDM processes in which the photon acts as a vector meson.

Contributions from the direct part and the anomalous part have been calculated in leading order pQCD by Owens[10]. The predictions for the contributions to the inclusive jet cross section from the various subprocesses at $\sqrt{s} = 19.4$ GeV and $y = 0$ are shown in figure 3. The direct coupling processes are expected to dominate for parton $P_t$'s above $\sim 5$ GeV; however, both components are appreciable at this $\sqrt{s}$ (for E683 $< \sqrt{s} > \sim 21.5$ GeV). The VDM contribution falls off rapidly for $P_t > 3$ GeV [10] and therefore is not expected to be appreciable for us.

The event topology for extended photon processes is expected to be different than that of the direct coupling processes due to the presence of the beam remnant. Extended photon interactions are expected to have four jets, two at high $P_t$ and the target and beam remnant jets.

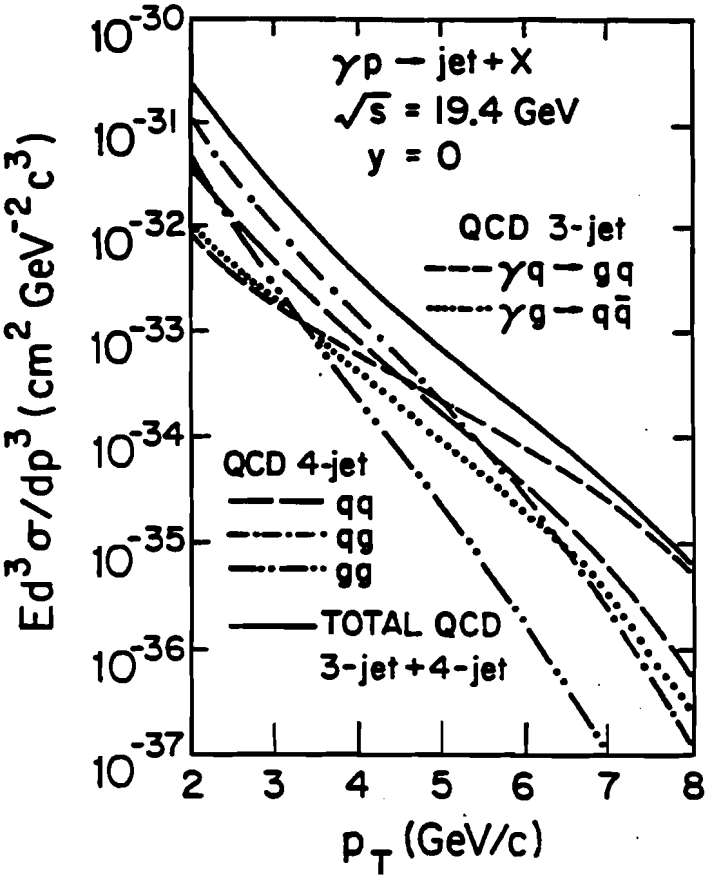


Figure 3: Predictions for the contributions to the cross section taken from reference [10] at $\sqrt{s} = 19.4$ GeV and $y = 0$ (y is the rapidity).

## 1.3 Fragmentation and Jet Physics

It is an experimental fact that free quarks have not been observed in nature. Isolated fractional charges - the signature of free quarks - have not indeed been observed in the almost 30 years since the quark model has been proposed. Instead, a parton struck with enough energy to escape from the 'asymptotically free' colorless state of a hadron, creates a stream of hadronic particles that are collimated along its direction. It is these 'jets' which are observed in experimental situations and not the partons themselves. The existence of hadron jets is taken as evidence for color confinement and is therefore considered a triumph of QCD.

The process of partons transforming into hadron jets is known as hadronization. Fragmentation applies to the complete process in going from partons to final state particles. This typically includes some particle decays. In principle, QCD should be able to give all the properties of jet fragmentation. Predictions for the flavor composition, multiplicity, and momentum distributions of particles in jets have, as yet, not been extracted from QCD.

The fragmentation of partons obscures the underlying hard QCD processes. The lack of exact information about how fragmentation proceeds has hampered the testing of pQCD predictions. Phenomenologically based models are used to compensate for the lack of calculable QCD based predictions. These models are used in a probablistic (i.e., Monte Carlo) approach for arriving at measurable

quantities. "jet universality" is assumed in implementing the models. This means the fragmentation process is assumed independent of the hard QCD process in which the partons are involved.

There are three main approaches currently used in the description of fragmentation. The most primitive (as far as predictive power) and the earliest proposed is the independent fragmentation model of Feynman and Field [11]. In this model the partons fragment independently of one another. The hadrons are formed by creating $q\bar{q}$ pairs of sucessive 'rank'. The first pair created forms the 'first rank' hadron with the parent parton. The remaining member of the pair forms the 'second rank' hadron with a newly created $q\bar{q}$ pair, and so on. Sucessive ranking hadrons are assigned a light cone fraction ($W = E - P_z$) according to a probability distribution, $f(z)$. Where $z$ is the fraction of the parent parton's light cone variable taken by the the hadron. This leaves a fraction $(1-z)$ for the higher ranking hadrons which are then treated iteratively in the same way. The flavor distribution of the created hadrons and the light cone fraction probability distribution are obtained from data.

It is clear that this model does not conserve energy or momentum. (nor does it conserve net quantum numbers such as electric charge , flavor, etc.). The model has no predictive power of its own and is mainly used to compare the sensitivity of the predictive power of other models.

The Lund string model applies a somewhat more sophisticated approach to the problem. We will describe it only briefly here. The details of the model are described in several references [12]. In the string model the partons exiting the hard scatter process are connected by a color flux tube - a string. Particles are created when the potential energy stored in the string , as the partons separate, exceeds the threshold to produce $q\bar{q}$ pairs. Each member of the pair forms another string with either end of the original string and more pairs are created until only on mass shell hadrons remain.

This model works well for systems in which there are no remnant partons. For example it works very well for modeling jets in $e^+e^-$ collisions. In such systems there is only one string (to first order) and it clearly must connect the two colored objects created in the annihilation. In a hadron-hadron system with remnant partons the string model does not reproduce the observed jet structures well. The inadequacy is thought to lie in the fragmentation of the remnant system and its concurrent interaction with the hard scatter system.

The final model that we will discuss, the cluster fragmentation model [12] [13] uses the approach of coherent parton showering. First we will discuss the fundamental concept of parton showering and later how it is applied in cluster fragmentation.

In general, higher order processes should also contribute to the event topology

in the 2→2 hard scattering processes we have been discussing and cannot be ignored. There are two approaches used to model these perturbative corrections. The matrix-element method involves calculating the Feynman diagrams order by order. The complexity of calculating these terms at higher orders limits the applicability of this approach. The other method, parton showering, while being only approximate, can be applied as sucessive branchings of the type 1→2 (for example; $q \rightarrow qg$, $g \rightarrow gg$, or $g \rightarrow q\bar{q}$). The probability for a parton to branch is given by Altarelli-Parisi evolution equations [14] (see also [47]).

The phase space for gluon emission increases with available energy. In parton shower modeling the amount of emission is characterized by a virtuality scale, $Q^2$ (which is controlled by the momentum transfer scale of the hard subprocess). Typically, the evolution is cutoff at some lower scale, $Q_o \sim 1$ GeV. The details of the modeling can be found in [41] or [47].

The cluster fragmentation model incorporates parton showering as the mechanism for fragmentation. The perturbative parton branching occurs as described above. The radiated gluons are then split non-perturbatively into $q\bar{q}$ pairs (also diquark-antidiquark pairs can be created). These are then recombined into color neutral objects called clusters. The massive clusters decay into hadrons - the number depending on the mass of the cluster and the available phase space for the production. These particles are then allowed to decay normally into the final

state jet particles.

Despite the many differences in the fragmentation models discussed, all are useful in modeling the data. Each will be used for comparision with data in this thesis. Furthermore, all have been tuned to reproduce final state measured distributions. The distinctions of the models at the particle level are subtle and beyond extraction from our data. New experiments must be devised to distinguish detailed predictions.

## 1.4 Nuclear Medium Effects

The study and understanding of nuclear medium effects on hard QCD processes has unique possibilities for obtaining information about parton interactions and behavior at short times after the initial hard scatter. ($< 10^{-23}$ seconds, i.e., before hadronization) [15]. The study of the space-time development of hadronization as well can at present best be studied using nuclear media [16].

In processes involving high momentum transfer a fast parton traverses the nucleus ($\gamma_{parton} \geq 5$). Hadronization is thought to occur outside the lorentz-contracted nucleus seen by the parton [15] [16]. The parton has a probability for subsequent interactions in the nuclear medium. This probability should be proportional to the amount of nuclear material that the parton sees which can be characterized by the atomic weight, A. Studying the effect of the nucleus on the

process involved as a function of A, can give information about the parton-nucleon cross section. In addition, it is clear that collective effects of nucleons on the QCD hard scatter process can be studied in this way.

Additional motivation for studying photon-nucleus collision comes from the fact that they have never been studied before. As discussed above, the direct photon interactions are simplified by the absence of a beam remnant in the final state and consequently will have cleaner jet signals that are easier to extract from the data. Qualitative predictions about nuclear dependence in photoproduction are already available [17].

Nuclear dependences in high $P_t$ single particle and jet production have been observed by numerous experiments studying hadron-nucleus collisions. They began with the discovery of the 'anomalous' nuclear enhancement of the cross section at high $P_t$ for single particle production by Cronin et al [18] in 1973. The ratio of single particle production cross section at high $P_t$ for nuclear targets to that for hydrogen, $(\sigma(pA)/\sigma(pp))$, was found to increase like $\sim A^{\alpha}$ with the power, $\alpha$, ranging from .8 up to 1.2 at a the highest $P_t$ measured of about 6 GeV. The value of $\alpha > 1$ is know as the anomalous nuclear enhancement effect.

Following this, the enhancement was also seen in jet production [19] [20] [21]. The values of $\alpha$ measured in jet production were even greater than seen in the single particle case. In jet production, $\alpha$ appears to depend on kinematic variables

such as $P_t$ and $\sqrt{s}$. However, it has recently been demonstrated that some of the available data must be corrected for azimuthal acceptance effects [22]. This may change some of the values of $\alpha$ reported and their dependences.

To date, the nuclear dependent phenomena in high $P_t$ production are not fully understood and any predictions available are qualitative. Here we will outline the accepted picture. It is expected that hard interactions, being rare, will occur anywhere inside the nucleus with equal probability. If this were the only consideration we would have $\alpha = 1$. The enhancement is thought to result from a rescattering of the partons exiting the nucleus in the final state. Partons entering the nucleus before the hard interaction could rescatter as well. Initial state effects appear, experimentally, to be small. The experimental evidence comes from studies of Drell-Yan production from nuclear targets which see only very small A-dependences [23]. However, there are predictions [24] that such initial state interactions should indeed be present in Drell-Yan.

Calculations based on probabilities for successive hard scatters [25] using parameterizations of the quark-nucleon cross sections [26] or gluon distributions in the nucleons [27] so far do not account for the enhancements seen. In these models the scattering is parameterized as

$$\sigma_{HARD} \propto c_0 A + c_1 A^{\frac{4}{3}} + c_2 A^{\frac{5}{3}} + ...$$

where $c_n$ is the probability of the $n^{th}$ hard scatter.

It was pointed out [24] that soft rescatters could be amplified in nuclear media. Higher order effects from interactions between partons and the spectators in the nucleus were predicted to have observable effects in Drell-Yan production occuring in a nuclear medium. An attempt was made to calculate these 'higher twist' effects for photoproduction of jets predicting a cross section enhancement as a function of A [17]. Specific predictions for kinematic dependences were also made.

We can think of the enhancement at high $P_t$ as partly due to soft rescatters with spectators partons in the nucleus. Because these effects cannot be calculated to all orders a parton shower approach may be useful here. The parton showering picture would require additional branchings in nuclear media. In other words, the effect can be thought of as an enhancement of the gluon radiation contributions in nuclear media.

In this thesis, measurements of nuclear enhancement for a kinematic variable that is related to $\alpha$ will be presented. $K_{t\phi}$ is defined in the last chapter (see section 5.1) as the out-of-plane component of the transverse momentum. $K_{t\phi}$ is more directly related to the mechanisms thought to be responsible for the nuclear enhancement in di-jet production than the cross section. The effect of a rescattering will show up as independent transverse momentum kicks to the outgoing partons or perturbations to their direction and will thereby show up as a broadening in the $K_{t\phi}$ distribution with A. The cross section for hard-scattering is an exponentially

falling function of $P_t$. The increased smearing of the $P_t$ by $K_{t\phi}$ as A increases also results in an 'apparent' enhancement in the cross section at high $P_t$ with A. Events from the highly populated $P_t$ regions are preferentially smeared into the sparsely populated tails leading to the enhancement at high $P_t$. A discussion of how $\alpha$ and $K_{t\phi}$ are related can be found in [22] and [28].

The out-of-plane component of the transverse momentum has particularly simple kinematic contributions. It can be easily measured in the lab frame since it depends only on the Lorentz-invariant transverse momentum vectors of the jets. Furthermore, it is a kinematic variable which is much less affected by the systematic uncertainties which can be present in cross section measurements (such as: flux uncertainties or target thickness dependent corrections).

# Chapter 2

# Description of the Experiment

## 2.1 Beamline

The Wideband beamline at Fermilab is the highest energy photon beam available to date. The data was taken using this tagged photon beam which was produced from a secondary electron beam via bremsstrahlung. To produce the photon beam from a primary high energy proton beam there are many intermediate steps necessary to alleviate neutral hadron contamination. A schematic of the beamline is shown in figure 4. Reference [29] discusses the design of the beamline in detail.

The primary beam of 800 GeV protons from the Fermilab tevatron was split and steered into various beamlines in the Fermilab fixed target area. This reduced intensity proton beam then impinged on a 3.5m long Deuterium produc-

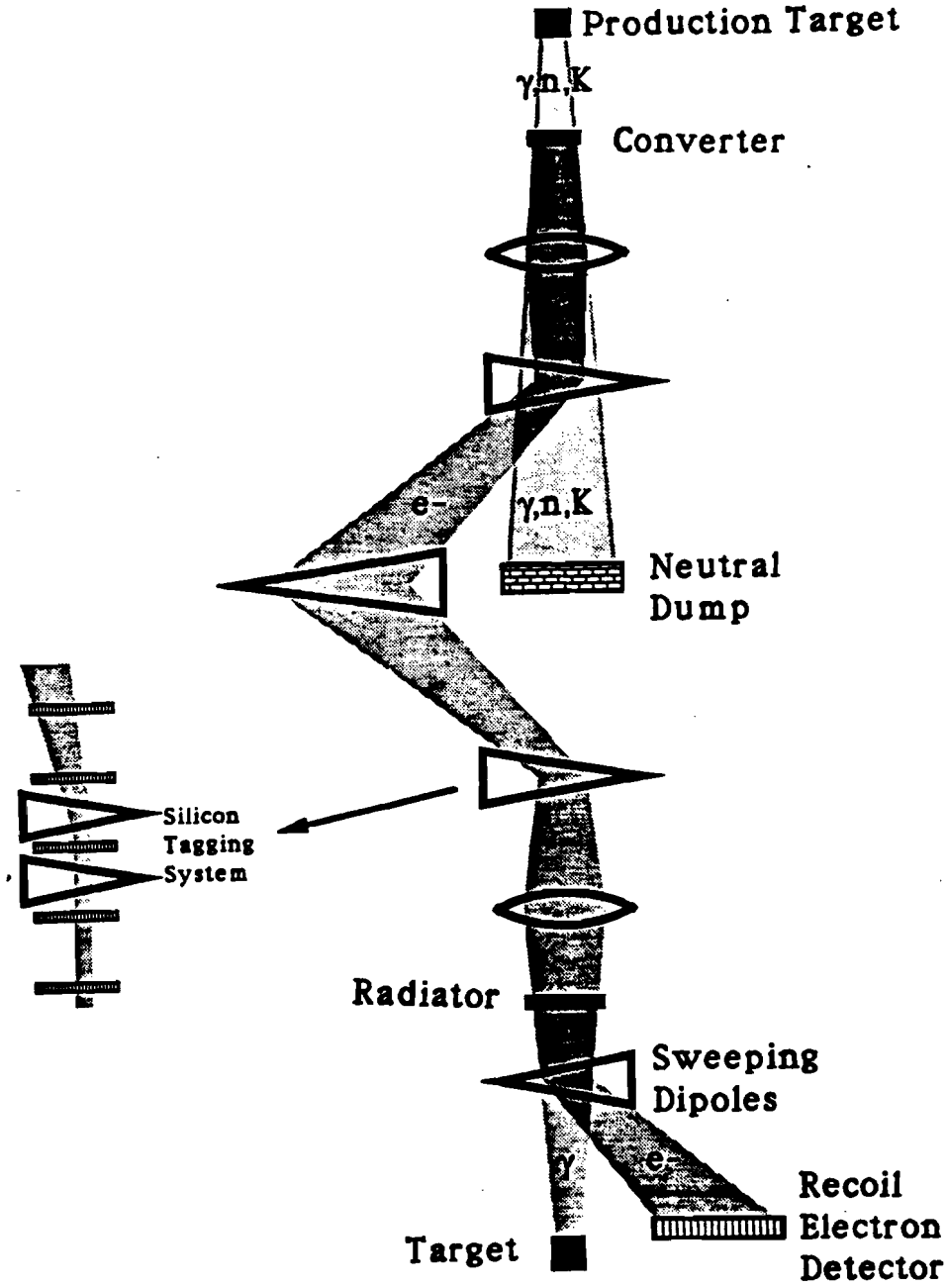


Figure 4: Wideband tagged photon beamline

tion target about 1km upstream of our experimental hall. The production target length and material were chosen to maximize the yield of high energy secondaries. Deuterium is optimal because of its low ratio of nuclear interaction length to radiation length. This property allows for a high yield of secondary particles due to both the high cross section for nuclear interactions and the decreased probability that the produced secondaries will have electromagnetic interactions on the way out of the target. Typically a mixture of charged and neutral hadrons including $\pi^o$, $\pi^+$,$\pi^-$,$K^+$,$K^-$, p, n, and $K_L^o$ emerged from the production target. The charged secondary particles were diverted with strong sweeping magnets and dumped while the neutrals (primarily photons from $\pi^o$ decay) passed through a thick ($\sim$ 50%) lead convertor. Resulting electron-positron pairs were steered around another dump and into a lead radiator producing the desired high energy photons from bremsstrahlung. (The beamline in principle can use both the electrons and the positrons to create bremsstrahlung photons but the positron system has not been successfully implemented as of this time due to contamination from positive hadrons, mainly protons and $\pi^+$ from upstream).

The primary proton beam was extracted from the Tevatron once every minute for a peroid of 23 seconds called a 'spill'. Within a given spill the primary beam was bunched by the accelerator RF (53MHz) into $\sim$3 ns wide buckets that were seperated by 18.8 ns intervals. The typical intensity of primary protons on the

production target was $3x10^{12}$ protons per spill. This produced a yield about $1.5x10^{8}$ electrons per spill and an average electron occupancy per RF bucket of $\sim$.19.

### 2.1.1 Photon energy tagging system

Due to the probabilistic nature of the bremsstrahlung process the photon beam had a broad energy spectrum. The photon tagging system was designed to measure the energy of each interacting photon. This required two detector systems. The first was the spectrometer which measured the momentum of the incident electron before bremsstrahlung. It consisted of five planes of silicon strips detectors seperated by two magnets. The layout is shown in the blowup in figure 4. Each plane contained 256 active microstrips having 300 microns width per strip. The electron trajectory was traced through this spectrometer and the momentum was determined from knowledge of the magnetic field. Events containing more that one electron in a bucket could easily be rejected by identifying multiple tracks in the spectrometer. The electron momentum distribution for our triggered data is shown in figure 5.

The microstrip system was built by FNAL experiment 687 and is described in reference [30]. The momentum acceptance of the spectrometer was about $\Delta p/p \pm$ 15%. It was capable of measuring the electron's momentum with a resolution of

about 2%.

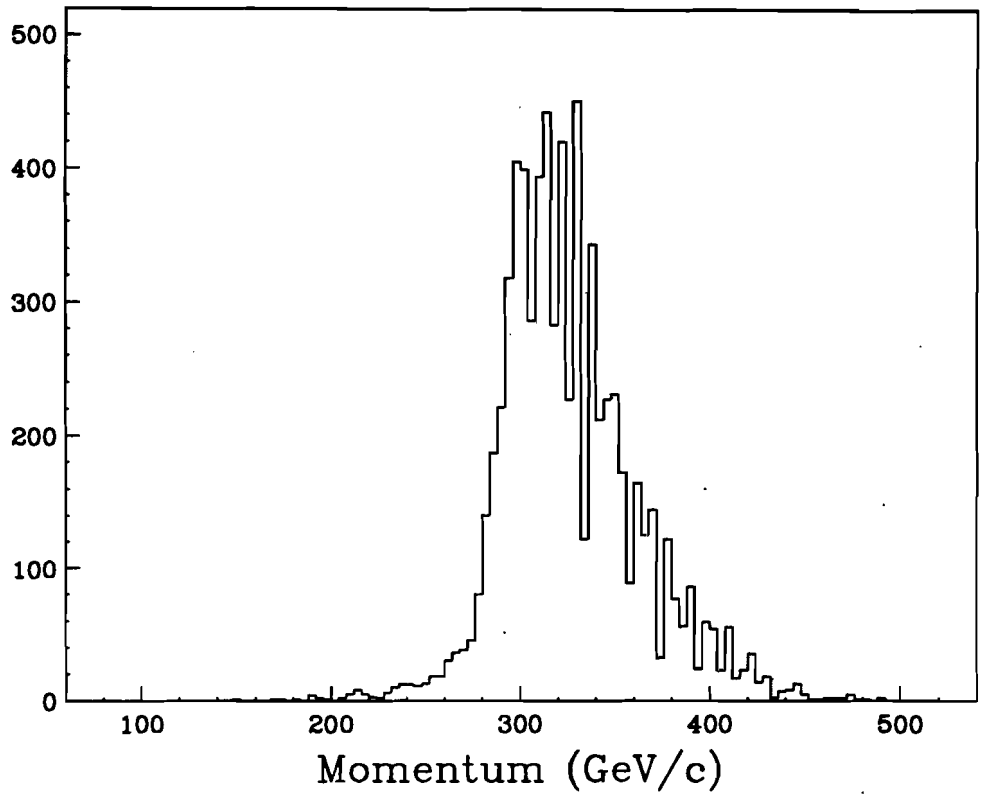


Figure 5: Incident electron beam momentum spectrum

Once the electron beam passed through the silicon strips it encountered a radiator (usually 20% of a radiation length of lead). Electrons and the photons they radiated (emerging with a very small opening angle which we neglected) were then seperated using a magnet. The photons continued forward to our target while the electrons were diverted into the RESH (Recoil Electron Shower Hodoscope). The RESH device was a series of 12 narrow ($\sim$ 2.5" wide) shower counters alligned

in the horizontal plane - perpendicular to the beam axis - at fixed z position with respect to the bend plane of the magnet (two of the counters were further upstream to improve the low momentum recoil electron acceptance). The recoil electrons were momentum analyzed by the magnet using the RESH elements as coarse position bins to measure the electron's deflection. A minimum energy deposition was required to trigger an element.

Table 2.1 shows the bin by bin energy tag for the recoil electron. The values shown were determined by comparison with a measurement of the photon's spectrum from an independent device - our forward total absorption calorimeter [32]. The tag bins are formed from the combinations of each hodoscope with either nearest neighbor or each alone. For example, shower hodoscope number 3 participates in three bins, 3⊕2 firing together is bin #4, 3 alone is bin #5, and finally 3⊕4 is bin #6 (⊕ here denotes a logical AND). Two nearest neighbor hodoscopes fire simultaneously when the electron hits near enough to their shared boundary that the shower occurs in both resulting in enough energy in each to pass the threshold requirement.

The tag bin population from our triggered data is shown in figure 6a. Hodoscopes 1 and 12 (corresponding to bins 1 and 23) have the largest energy acceptance. (counter 12 is physically the widest ~16"). Tag bin 1 has additional counts from stray particles resulting from its proximity to the beampipe and the

| Tag bin | Hodoscope logic | $E'_e$ (GeV) | $\delta E$ $\pm 1$ ($GeV$) |
|---|---|---|---|
| 1 | 1 | 229.7±2.3 | 19.5* |
| 2 | 1⊕2 | 187.7±1.9 | 14.9 |
| 3 | 2 | 163.5±1.6 | 12.8 |
| 4 | 2⊕3 | 144.9±1.4 | 13.1 |
| 5 | 3 | 129.8±1.3 | 10.2 |
| 6 | 3⊕4 | 119.4±1.2 | 10.3 |
| 7 | 4 | 107.7±1.1 | 10.8 |
| 8 | 4⊕5 | 99.7±1.0 | 10.1 |
| 9 | 5 | 91.6±0.9 | 12.0 |
| 10 | 5⊕6 | 86.9±0.9 | 11.9 |
| 11 | 6 | 81.1±0.8 | 13.2 |
| 12 | 6⊕7 | 76.5±0.8 | 10.7 |
| 13 | 7 | 71.8±0.7 | 12.6 |
| 14 | 7⊕8 | 68.4±0.7 | 11.4 |
| 15 | 8 | 63.7±0.6 | 12.1 |
| 16 | 8⊕9 | 61.4±0.6 | ** |
| 17 | 9 | 57.9±0.6 | ** |
| 22 | 11⊕12 | 53.3±1.0 | 11.5 |
| 23 | 12 | 30.1±0.3 | 16.8 |

Table 2.1: RESH tag bin energies. $E'_e$ is the energy of the electron that hits the geometric centerline of the hodoscope configuration, $\delta E$ is the half width of the bin. (bins 18-21 are absent because hodoscope #10 is occluded by the magnet pole and hodoscope #11 does not count independently of #12.)
* geometric contribution only
** not measured

beam dump (where non-radiating electrons were deposited).

The RESH detector dominated the photon tag resolution. The resolution shown in the table is on average about 5%. The geometrical widths of the counters are not an important contribution to the resolution. The dominant contribution to the width may be due in part to off axis beam particles and/or beam divergence. The precise cause is currently under study.

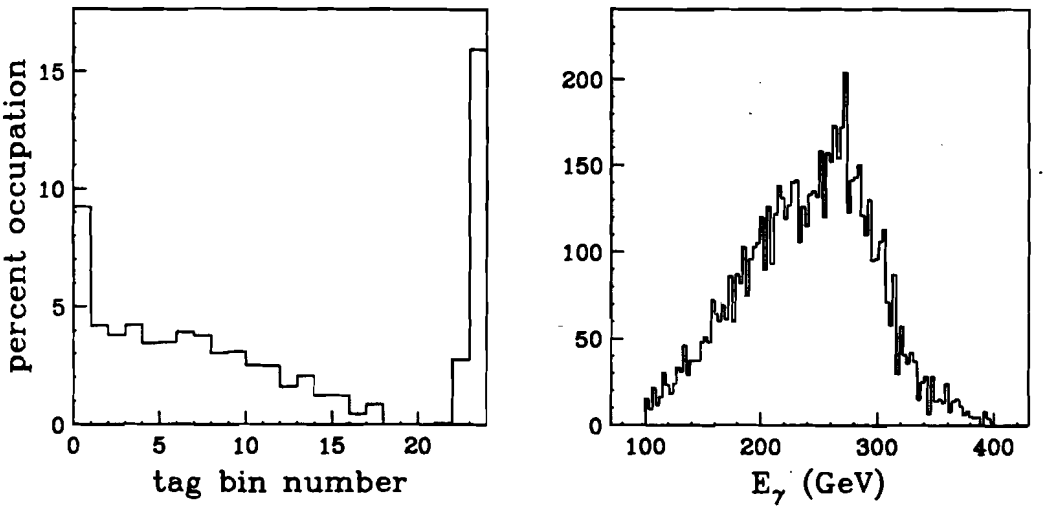


Figure 6: a.) Triggered tag bin population for RESH detector. b.) Photon energy spectrum measured by the tag system.

The triggered photon energy spectrum is shown in figure 6b. It is computed from the difference in the recoil electron's energy measured from the RESH detector, $E'_e$, and the incident electron's energy as measured by the silicon strip spectrometer, $E_e$.

$$E_\gamma = E_e - E'_e$$

The geometric acceptance of the RESH system selects the range and has the desired effect of hardening the bremsstrahlung spectrum.

## 2.2 E683 detector

### 2.2.1 Overview

A overview of the 683 detector is shown in 7. The experiment was designed primarily to measure energy flow. As such, the two main components of the detector were calorimeters. The wide angle calorimeter, MCAL (for Main CALorimeter) sat about 300" downstream of the target. It had full azimuthal acceptance and covered a polar angle acceptance of $20° < \theta^* < 120°$ at $\sqrt{s} = 21$ GeV. The MCAL had a 8" by 8" hole in the center allowing the noninteracting beam particles and the forward going reaction products to be deposited in the BCAL (for Beam CALorimeter). In this section we will proceed to discuss each component of the detector in some detail.

### 2.2.2 Main Calorimeter

The MCAL detector was relied upon to provide most of the information about the high $E_t$ interactions. Its segmentation allowed sensitivity to the angular energy flow in the reaction and its layering provided some identification of the particles

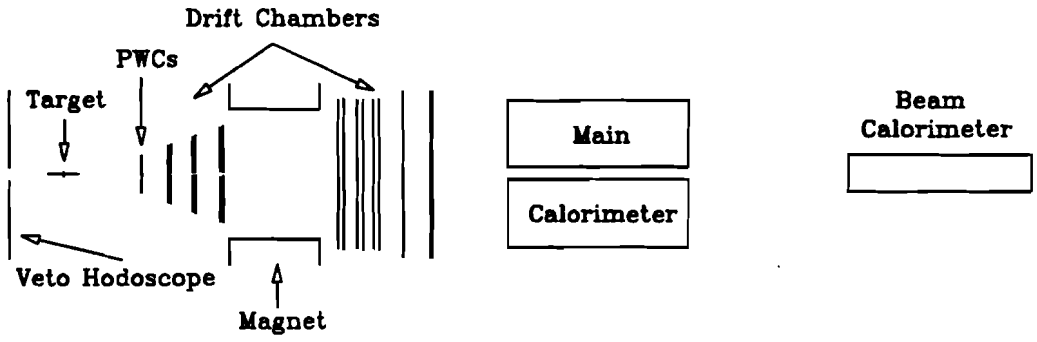


Figure 7: E683 detector (top view)

produced. It was originally used in Fermilab E609 (hadroproduction of high $P_t$ jets) and its design considerations are discussed in several references (see [31]).

Figure 8a shows the segmentation of the MCAL's face. Each layer is segmented into 132 modules. The modules, one from each layer, whose centers line up to point at the target are associated to form a 'tower'. Each tower subtends $\Delta\eta \simeq 0.18$ and $\Delta\phi \simeq 0.26$ rads, where $\eta$ is the pseudorapidity, $\eta = -\log\tan\frac{\theta}{2}$, determined from the polar angle $\theta$ and $\phi$ is the azimuthal angle.

The MCAL's four layers in depth can be seen in figure 8b. Layer A′ modules consist of slices of lead alternated with scintillator amounting to a total of 5-8.5 radiation lengths. The same layer amounts to only about .5-.9 nuclear interaction lengths. Layer A, B, and C are composed of iron alternating with scintillator sections. These layers add to about 6-8 nuclear adsorption lengths. The thickness of layers is decreased at the wider angles to compensate for the kinematic relation

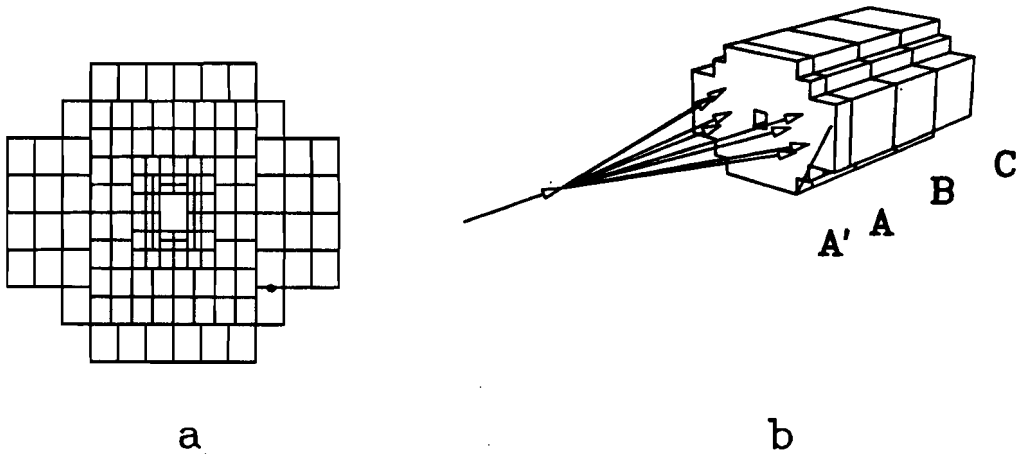


Figure 8: a.) Face of the MCAL showing segmentation. b.) 3D view of MCAL showing the four layers.

of decreased energy for fixed $E_t$ particles at wider angles (larger $\theta$).

The four layers discussed above, A′, A, B, and C were designed to distinguish electromagnetic showers from hadronic showers by using the differences in the longitudinal shower developement for the two cases. An Electromagnetic shower will be contained in the first two layers, A′ and A. It will rarely deposit any of its energy in the last two layers, B and C. This means that energy in the B and C layers can be identified as resulting from hadronic showers. The energy in the first two layers is somewhat more complicated because on average you can expect that hadronic showers will drop from about $20\% - 40\%$ of their energy in layer A. However, one can still distinguish events which have all or large fraction of their energy in layers A′ and A as being electromagnetic.

There is generally a mixture of both hadronic and electromagnetic type particles in a given jet event. Layer A can contain a sizeable fraction on average of energy from each type of shower. Our calorimeter is of a type known as 'non-compensating'. Energy in a detectable form (i.e., photons seen by our PM tubes) from sampled hadronic showers is about a factor of .8 less than that from electromagnetic showers created from a shower originator of the same energy . (Calorimeters that see the same signal response from both types of showers are called 'compensating'). Because we do not know on an event by event basis what fraction of each type of energy is deposited in layer A, there is an ambiguity in assigning a calibration factor to it. At the moment we assign all energy in layer A as electromagnetic. The additional width associated with assigning a single calibration factor to this layer is incorporated in the quoted resolution. (This effect was pointed out by D. Lincoln [33]). It is estimated that our overall energy scale is systematically 10% low due to this effect [33].

The detector was calibrated with $e^-$'s and $\pi$'s at various energies. In addition straight through beam halo $\mu$'s were used to initially balance the signal from each of the 532 phototubes to a relative 5% accuracy. The final calibration pass is still underway. The resolution quoted for this analysis reflects the current state of the uncertianty in the calibration factors. The resolution is estimated to be $35\%/\sqrt{E} \oplus 3\%$ for electromagnetic energy and $75\%/\sqrt{E} \oplus 10\%$ for hadronic

energy (where '$\oplus$' symbolizes addition in quadrature).

### 2.2.3 Wire Chambers

The chambers will eventually be used to track the particles from the interaction and to reconstruct an interaction vertex. Tracking is not presently implemented but the chambers will be discussed for completeness.

The first 5 planes are MPWC's (multiwire proportional wire chambers).The signal output for a wire that had charged particles pass within its active cell is proportional to the charge. This results in a signal from each wire specifying the number of charges that hit its active cell, if any, per event. These detectors had a wire spacing of 1.95mm which determined the resolution of their position measurement.

The remaining 6 upstream planes as well as the 13 planes downstream of the magnet were drift chambers. Drift chambers can resolve distances within the active wire cell by measuring drift times. Drift times result from the fact that the charges, created by the ionization of the gas when a charged particle passes through it, drift towards the anode wire in the electric field. The time it takes is a function of the electric field, the type of gas, and its pressure. The distance that the ionization charges traveled in the cell associated with a given wire can then be determined by measuring this drift time. In general, since the electric field in

the cells is not uniform, the relationship of the drift time to the drift distance is not linear. The chamber's position measurement accuracy is ultimately limited by how well the time to distance function can be known. In addition to depending on the diffusion properties of the gas and fluctuations in local gas pressure, for us it is more likely dominated by the pulse rise times of the signals from the wires and jitter in the triggering signal pulse. Based on inherent $\delta t \sim 5$ nsec in our trigger timing, the position resolution of the drift chambers is estimated to be .5mm.

The time to distance functions for the largest drift planes, the 'Monster chambers', (drift planes 13-19) were fitted as polynomials on a plane by plane basis. These chambers have a wire spacing of 0.75". They consist of three X measuring planes (144 wires on each) and two of each U and V planes (192 wires on each) with a slant angle of 15°. They were operated in the plateau region with a gas mixture of 50% Argon with 50% ethane maintained at a constant pressure of 0.07 ($\pm$0.02) inches of water above atmosphere. The fit coefficients for the various planes are shown in table 2.2.

A TDC spectrum for a typical wire is shown in figure 9. The horizontal axis measures the time between the 'start', provided by a signal on the wire and a 'stop' from the event trigger. The function x(t) is obtained by fitting the integrated TDC spectrum using the relation:

$$x(t) = C \int_{t_o}^{t_{max}} \frac{dN}{dt}\, dt$$

Which is obtained from:

$$\frac{dN}{dt} = \frac{dN}{dx}\frac{dx}{dt} = \frac{N}{h}\frac{dx}{dt}.$$

Where $\frac{dN}{dt}$ is the TDC spectrum for the cell and $\frac{dN}{dx}$ is a constant ($=\frac{N}{h}$) for a uniformly illuminated drift cell. N is the number of hits in the cell and h is the cell width (= wire spacing/2). From the above expression the importance of $t_0$ and $t_{max}$, the minimum and maximum drift times in the cell are apparent. The intrinsic timing uncertainty in the trigger limits how well these can be determined. The three regions of the fit correspond to time slices in the TDC spectrum.

$$\text{I} \quad 0 < t < 40ns$$

$$\text{II} \quad 40 < t < 180ns$$

$$\text{III} \quad 180 < t < 200ns$$

Where $t = t_o - t_{TDC}$ is the drift time. (Note that $t_o > t_{TDC}$ in the common STOP mode TDC readout configuration).

The magnet in conjunction with the tracking will be used to determine leading particle charge in the jets. The magnet has a $P_t$ kick of about 70 Mev. This small $P_t$ kick was chosen so that the jet shapes would not be distorted and the jet $P_t$'s would not be measurablely affected by it. We neglect the effect of the magnet in reconstructing the jet $P_t$'s.

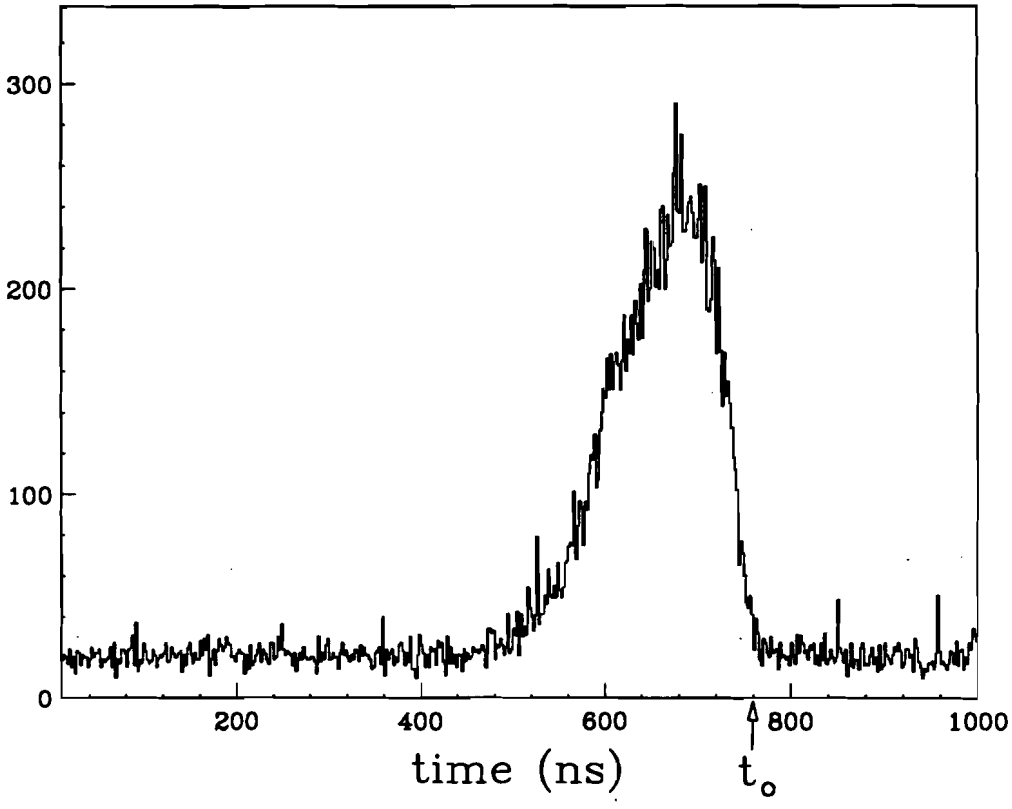


**Figure 9: TDC spectrum for a typical wire in the Monster Chambers.**

| Region of fit | Plane # | $A_0$ (mm) | $A_1$ (mm/nsec) | $A_2$ (mm/nsec$^2$) | $A_3$ (mm/nsec$^3$) |
|---|---|---|---|---|---|
| I | 13 | $2.53\text{x}10^{-2}$ | $1.74\text{x}10^{-2}$ | $1.67\text{x}10^{-3}$ | $2.53\text{x}10^{-5}$ |
| | 14 | $1.92\text{x}10^{-2}$ | $1.84\text{x}10^{-2}$ | $1.02\text{x}10^{-3}$ | $2.53\text{x}10^{-6}$ |
| | 15 | $7.80\text{x}10^{-3}$ | $6.81\text{x}10^{-3}$ | $1.08\text{x}10^{-3}$ | $2.53\text{x}10^{-6}$ |
| | 16 | $5.24\text{x}10^{-3}$ | $3.45\text{x}10^{-3}$ | $5.64\text{x}10^{-4}$ | $2.53\text{x}10^{-6}$ |
| | 17 | $5.02\text{x}10^{-3}$ | $4.99\text{x}10^{-3}$ | $1.82\text{x}10^{-3}$ | $2.53\text{x}10^{-5}$ |
| | 18 | $9.34\text{x}10^{-3}$ | $8.53\text{x}10^{-3}$ | $1.29\text{x}10^{-3}$ | $2.53\text{x}10^{-6}$ |
| | 19 | $7.23\text{x}10^{-3}$ | $-2.71\text{x}10^{-3}$ | $1.46\text{x}10^{-3}$ | $2.53\text{x}10^{-5}$ |
| II | 13 | $-5.55\text{x}10^{-1}$ | $7.48\text{x}10^{-2}$ | $-1.21\text{x}10^{-4}$ | 0 |
| | 14 | $-9.92\text{x}10^{-1}$ | $8.47\text{x}10^{-2}$ | $-1.53\text{x}10^{-4}$ | 0 |
| | 15 | -1.43 | $8.40\text{x}10^{-2}$ | $-1.34\text{x}10^{-4}$ | 0 |
| | 16 | -2.36 | $9.27\text{x}10^{-2}$ | $-1.61\text{x}10^{-4}$ | 0 |
| | 17 | -0.87 | $7.77\text{x}10^{-2}$ | $-1.31\text{x}10^{-4}$ | 0 |
| | 18 | -1.08 | $8.34\text{x}10^{-2}$ | $-1.43\text{x}10^{-4}$ | 0 |
| | 19 | -1.85 | $9.20\text{x}10^{-2}$ | $-1.66\text{x}10^{-4}$ | 0 |
| III | 13 | -5.14 | $1.26\text{x}10^{-1}$ | $-2.67\text{x}10^{-4}$ | 0 |
| | 14 | -1.39 | $9.87\text{x}10^{-2}$ | $-2.21\text{x}10^{-4}$ | 0 |
| | 15 | -0.74 | $9.23\text{x}10^{-2}$ | $-2.04\text{x}10^{-4}$ | 0 |
| | 16 | -8.30 | $1.63\text{x}10^{-1}$ | $-3.70\text{x}10^{-4}$ | 0 |
| | 17 | -16.4 | $2.39\text{x}10^{-1}$ | $-5.49\text{x}10^{-4}$ | 0 |
| | 18 | -2.60 | $1.12\text{x}10^{-1}$ | $-2.54\text{x}10^{-4}$ | 0 |
| | 19 | -6.35 | $1.52\text{x}10^{-1}$ | $-3.60\text{x}10^{-4}$ | 0 |

Table 2.2: Drift time to drift distance function fits for the Monster Drift Chambers. The polynomial functions have the form $x(t) = A_0 + A_1 t + A_2 t^2 + A_3 t^3$ with $A_3 = 0$ in regions II and III.

### 2.2.4 Forward Calorimeter and Pileup Monitor Device

The second detector needed to cover the forward region ($0° < \theta^* < 20°$) was the BCAL. It sat a few feet downstream of the MCAL with lateral dimensions 2' by 2'. It consisted of four sections of iron-scintillator sandwiches. Each of the first two sections has $\sim$ 12 radiation lengths and each of the remaining two has $\sim$35 radiation lengths. Light output from each section was collected by two phototubes. The design details are discussed in the reference [34]. This detector also suffered from the effects of noncompensation. In this case, the sampling was done in each layer with iron. Iron has about three times larger radiation length than lead so the first two sections needed to be made thick to contain the electromagnetic showers. The additional interaction length in section 1 caused the hadronic showers to start earlier in general. This resulted in section 2 containing sizeable fractions on average of both types of showers. (The calibration factor for section 2, in this case, was adjusted so that the total energy was correct on average[35]). In addition, as discussed below, our forward energy had several components.

This calorimeter had a number of demands on it. It was designed to be used to study all of the following:

1. Forward energy from the high $P_t$ reaction.

   This includes contributions from both remnant jets as well as spillover from high $P_t$ jets.

2. The non-interacting forward energy in the event.

This resulted from multiple bremsstrahlung in the radiator and upstream.

3. The flux of the photon beam and its spectrum.

The contribution from multiple bremsstrahlung directly adds to the forward energy flow in the event. On an event by event basis, the small difference in the remnant jet energy is washed out by the uncertainty in the magnitude of this contribution. This problem will be discussed more later but it should be noted that the seperation of the multiple bremsstrahlung contribution has not been accomplished on an event by event basis to date.

The problems associated with item 3 have both been solved and will be explained further here. Because the BCAL directly absorbed the non-interacting beam flux it suffered radiation damage to the scintillators through the course of the data taking peroid. The loss in pulse height with time has been determined from calibration data taken at various intervals during the run. It is a well understood time dependent correction to the BCAL energy[35].

The high rate 'in beam' environment has associated with it the additional complication of beam pile up. For us, since events with electrons in the same beam bucket can be eliminated through tracking in the tag spectrometer, we are concerned with the problem of electrons in beam buckets nearby to the trigger bucket. This was a problem because the BCAL PM signals were typically 60ns

long. The ADC gate used to integrate the pulse was 80ns long. The presence of electrons in any of the two buckets before or the three buckets after the triggered event could include spurious signals in the ADC gate. In order to be able to select data events which were free from this type of pile up in the BCAL we devised a 'pileup monitor'. It consisted of two planes of very thin scintillator (to minimize mass that is directly in the electron beam) with a fast phototube/base system to respond to each beam bucket. The signal were in addition clipped to $\sim$ 15ns insure that the system recovered within one beam bucket.

These signals were read out by two devices. One device was a simple latch which had as input 8 signals for each plane consisting of the signals -4,-3,-2,-1,+1,+2,+3,and +4 buckets out of time with the trigger bucket respectively. They correspond to pile up four buckets on either side of the trigger bucket. There was in addition a multihit TDC which was able to measure the timing of three bucket signals with respect to the TDC start (trigger bucket). This device used the two planes in 'AND' mode. Figure 10 shows the readout signals for the two devices. Both readout methods proved consistent and were used sucessfully to eliminate events with pile up in offline analysis. The performance of this device is also discussed in [36].

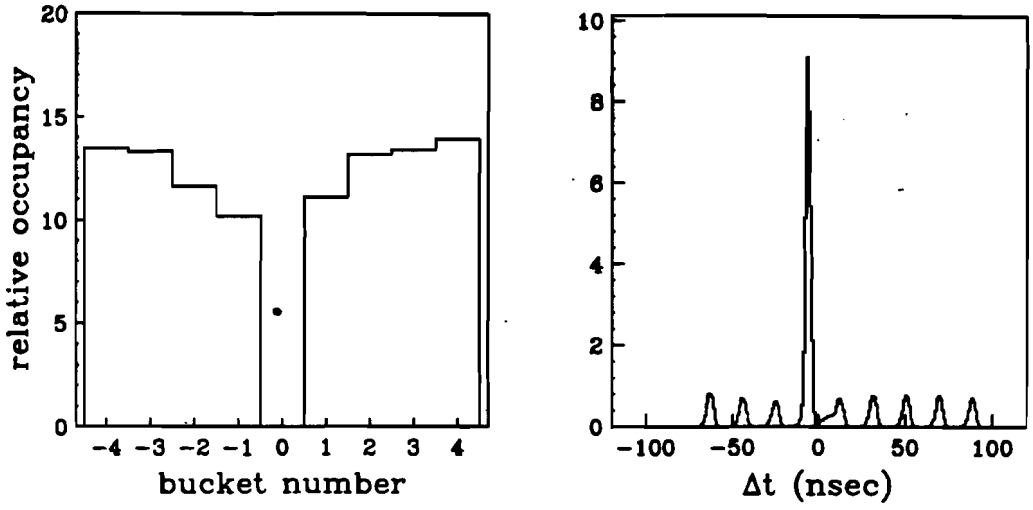


Figure 10: a.) bucket hitmap shows the occupancy of surrounding beam buckets. b.) multihit TDC spectrum of the beam particles.

### 2.2.5 Targets

Our targets included two cryogenic targets, liquid Hydrogen and liquid Deuterium, as well as six solid nuclear targets. They are described in Table 2.3. Only one of the two cryogenic targets was available at any given time. The same cryogenic target vessel was used for each, requiring a warmup and venting of the target vessel each time a switchover was performed. The nuclear targets were mounted on a wheel which could rotate to place a different target in the path of the beam. This wheel and the cryogenic target vessel were mounted on a transporter that travelled horizontally allowing either to be place in the beam easily.

The targets were alternated to reduce the A-dependence measurement sys-

tematics. The cryogenic liquid target was alternated once per ~60,000 triggers (about four hours of data taking) with the nuclear target wheel. About 30,000 data triggers were then taken on the nuclear targets (which were changed every spill by rotating the wheel). This cycle was repeated throughout the data taking peroid with a liquid target changeover occuring four times. In addition, about 10% of our data was taken with a $\pi^-$ beam on all the targets. This pion beam data was taken at various times during the run for a several day peroid each time.

The cryogenic target vessel could be emptied to a resevoir (from which we could refill it) with a turnaround time of about 1 hour. We did this every 4 or so cycles of the liquid/nuclear alternation to obtain empty target vessel data (about 15,000 events per empty/fill cycle). For the nuclear targets, the blank target (one of the positions on the target wheel) gave us information about the non-target related events.

## 2.3 Triggering

The purpose of our trigger was to select events in which a hard scatter occurred on partons in our target. These events are characterized by the relatively high $E_t$ of the exiting particles. The bulk of the interactions taking place are not hard scatters. To minimize the computer dead time that would result from recording all the interactions taking place we choose a trigger which selected only events

| Target | Atomic weight | Thickness (cm) | Nuclear interaction lengths (cm) |
|---|---|---|---|
| $LH_2$ | 1.0 | 50.75 | .071 |
| $LD_2$ | 2.0 | 50.75 | .150 |
| Be | 9.0 | 2.54 | .062 |
| C | 12.0 | 2.54 | .067 |
| Al | 27.0 | 2.00 | .051 |
| Cu | 63.6 | 0.61 | .041 |
| Sn | 118.7 | 0.50 | .022 |
| Pb I | 207.2 | 0.37* | .022 |
| Pb II | 207.2 | 0.13 | .007 |

Table 2.3: E683 Targets.
*a thicker Pb target (.75cm) was used for a short time during the run.

having sufficiently high $E_t$. The segmentation of the MCAL provided energy concentration descrimination so that we could measure the 'vectorlike' quantity $E_t$ for each event.

A hardware trigger based on the $E_t$ in the MCAL was accomplished in the following way. The energy for each tower, $E_i$, was formed from the energies of the associated module in each layer $(A_i', A_i, B_i, C_i)$ as the sum:

$$E_i \;=\; .8A_i' + .8A_i + \; B_i + \; C_i \quad i = 1,132$$

This was to de-weight appropriately the primarily electromagnetic modules in the triggering since they are enhanced by their increased light output. Failure to do this would result in a slight trigger bias toward EM heavy events. The energy from each tower, $E_i$, was then attenuated by $\sin\theta_i$ to form a signal proportional to $E_{ti}$ for the tower. Different logical combinations from the tower $E_{ti}$'s were then constructed to make up our three interaction triggers.

The three triggers were used concurrently in the data stream in an 'OR'ed configuration. The triggers were:

**TWOHI** any two towers above a threshold value ($\sim$ .75 GeV)

**GLOBAL** the total $E_t = \sum E_{ti}$ $i = 1,132$ above a threshold value ($\sim$ 7 GeV).

**TRIGGER MATRIX** an 'OR' of 40 different kinematically correlated solid angle patterns that were programmed into a logic circuit.

The processing time for the trigger logic (as well as the signal amplification and propagation) were offset by a fast 'pretrigger' system. The requirements for a 'pretrigger' were $\overline{(C1 \oplus B1)} \oplus C2$ (the symbol $\oplus$ here signifies a logical 'AND') and also enough total $E_t$ in the MCAL to pass a minimum 'GLOBAL LOW' $E_t$ threshold (>5 GeV). C1 and B1 were two fast rise time scintillation counters placed just before our interaction target and C2 was place just after it. The presence of this 'pretrigger' and the absence of a computer busy vetoed subsequent 'pretrigger' candidates until the second level decision we called the 'master gate' could be processed. The presence of a 'master gate' prevented the release of a fast clear which reset the 'pretrigger'.

There were two important vetoes to the 'master gate' signal. The purpose of both was to reduce the fake high $E_t$ triggers that could result from either of two sources. One source was from beamline halo muons which originated from decay of pions that were produced in the primary production target (see section 1 of this chapter). The muons do not deposit much energy but can have substantial $E_t$ if they produce a knock on $\delta$-ray or bremsstrahlung in the wide angle wings of the MCAL. The other source of fake high $E_t$ triggers was from phototube breakdown in the MCAL. The GLOBAL trigger in particular was susceptible to these fake triggers.

The beamline muons were detected using a veto wall just before the target that

shadowed the face of the MCAL. This was used directly to veto those events which had an associated beamline muon. There were two walls of paddles used in 'AND' mode. The large size of the individual paddles (about 1' x 4') contributed to the slow signal rise times and as a result the veto was not completely efficient (estimated efficiency $\sim 95\%$). The 'ONE-HI' veto recovered some of the inefficiency of the hodoscope and could also veto phototube breakdown type events. It vetoed events that had one and only one hot tower in the MCAL but enough total $E_t$ to pass the GLOBAL trigger requirement. These hardware vetoes served to reduce the deadtime from the fake high $E_t$ events however did not completely eliminate them from the data sample. Additional software cuts (that will be discussed in the analysis section) were needed.

We had an additional type of trigger know as the 'flux monitoring triggers'. These were prescaled and readout in the data stream concurrently with the high $E_t$ triggers. Their purpose was mainly for system diagnostics, for example gain stability monitoring and online monitoring of detector system efficiency and malfunction. Events from these triggers contributed little to the deadtime (less than 10%). In addition, they were used for a calibration study of the photon tag system. These triggers included:

**RESH** required a signal above the energy threshold in any of the RESH hodoscopes.

**BCAL** required > 100 GeV energy in the BCAL.

**PAIR** required at least double minimum ionizing signal in the post target trigger counter C2 and also $\overline{C1}$.

**LED** triggered by a low rate pulser which is sent to pulse the LED's mounted on each of the MCAL phototubes (used for gain stability monitoring).

## 2.4 GEANT Study of Photon Beamline

As mentioned earlier in this chapter one of the major sources of uncertainty in the measurement of our forward going interaction energy is the contribution from non-interacting photons created by multiple bremsstrahlung in the radiator. The multiple bremsstrahlung in the radiator also creates a source of uncertainty in determining the interacting photon's energy. In an effort to quantify our understanding of these effects a Monte Carlo GEANT simulation of part of the beamline was undertaken. Some results from that study will be presented here.

In general, when a fast electron passes through matter it can bremsstrahlung several times depending on the thickness of the material involved. The more material it passes through the greater chance it has to radiate photons. This complicated the tag photon energy measurement in the following way. Suppose an electron passing through our radiator has bremsstrahlunged twice, emitting

two photons having energies $E_1$ and $E_2$ respectively. One of the photons, the one with energy $E_1$, interacted in our target generating an event trigger. The tag photon energy measured for the event would be larger than the interacting photon energy by the amount $E_2$, the energy of the non-interacting photon. In principle, our detector could measure $E_2$ in the forward beam calorimeter and we could reconstruct the 'true' triggering photon's energy. In practice, this requires seperating the unreacting photon beam energy from the triggered event forward energy flow (a large fraction of which is usually hadronic in nature and penetrates deeper into the BCAL than the photon).

Further complications arise from the details of the detector's environment. The experimental hall was about 100m long. The 683 detector sat at the far end of the hall rougly 80m from the fixed radiator. Between the radiator and our detector was another operating experiment's detector (E687). It consisted of material amounting to a total of about $0.25X_o$ (25% of a radiation length) and also included two rather high $P_t$ kick magnets (0.4 GeV and 0.8 GeV). The concern was that the non-interacting photons could pair produce in this material and be swept out of the beamline by the high $P_t$ kick magnets. We could then have no chance of reconstructing the 'true' triggering photon's energy.

GEANT[37] was used to simulate the energy loss and interactions of the photons in the beamline from the radiator to our target. All passive material, limiting

aperatures and magnets were included in the simulation. These are shown in table 2.4. DET1 and DET2 are the points where the energy spectrum and its composition were determined. Events were vetoed if charge was present at these points as discussed below.

A monochromatic 350 GeV electron beam was passed through the radiator (this study was done with each of 10%, and 20% radiator thicknesses). The bremsstrahlung events which had recoiling electrons with energy outside of the RESH energy range ($20< E_e' <210$ GeV) were vetoed at this point. This resulted in a photon beam energy range of $140< E_\gamma <330$ GeV. In events which passed this requirement the recoiling electrons were stopped in the RESH detector. The photons were allowed to continue on through the beamline. The first active element, DET1, was placed just after TGT (E687's target) and VTX, their vertex detector. Material upstream of this point amounted to about $0.15X_o$, $\sim$ 60% of the material in the beam. Events in which charge was present in DET1 were vetoed (with 100% efficiency). Events which survived were allowed to proceed through the remaining material, aperatures, and magnetic fields. The energy spectrum and composition were determined again at DET2 which was located just before our experiment's target. Events which had charged particles at DET2 were also vetoed. The additional requirement was made at DET2 that there be at least one 'hot' (> 100GeV) photon present. Only such energetic photons can cause high $E_t$

| Distance from Radiator (cm) | Name | Material | Number of Radiation lengths | Description |
|---|---|---|---|---|
| 0 | RAD | Pb | .1,.2 | passive |
| 786 | MAG0 | He | .0017 | passive. |
| 1756 | RESH | - | 0 | detector,veto |
| 2256 | TR0 | lucite | .0036 | passive |
| 2286 | TGT | Be | .1 | passive |
| 2316 | TR1 | lucite | .0036 | passive |
| 2319 | VTX | Si | .036 | passive |
| 2320 | DET1 | - | 0 | detector,veto |
| 2321 | TR2 | lucite | .0036 | passive |
| 2536 | MAG1 | He | .0003 | MAGNET $P_{tkick} = +0.4GeV$ |
| 2676 | P0 | mylar | .0061 | passive |
| 2686 | C1W | quartz | .0006 | passive |
| 2837 | C1G | He | .0031 | passive |
| 2988 | C1B | quartz | .0099 | passive |
| 2991 | P1 | mylar | .00675 | passive |
| 2996 | C2W | quartz | .0006 | passive |
| 3147 | C2G | $N_2$ | .01 | passive |
| 3298 | C2B | quartz | .014 | passive |
| 3361 | P2 | mylar | .0061 | passive |
| 3491 | MAG2 | air | .0055 | MAGNET $P_{tkick} = -0.8GeV$ |
| 3806 | P3 | mylar | .00675 | passive |
| 3836 | C3W | quartz | .0006 | passive |
| 4176 | C3G | He | .0014 | passive |
| 4511 | C3B | quartz | .0206 | passive |
| 4516 | P4 | mylar | .00675 | passive |
| 4674 | IE | air | .0015 | aperature |
| 4839 | HC | air | .0043 | aperature |
| 5220 | MS | air | .0032 | aperature |
| 5400 | DET2 | - | 0.0 | detector,veto |

Table 2.4: Beamline Material and active elements included in GEANT simulation. *Not implemented as a Magnet here (instead energies of electrons entering the RESH detector are known exactly, electrons are then prevented from proceeding).

| $\delta$ (GeV) | Fraction with $E_{tag} - E_{hot} < \delta$ | Fraction with $E_{tag} - E_{total} < \delta$ |
|---|---|---|
| 5 | .37 | .60 |
| 10 | .47 | .67 |
| 15 | .53 | .72 |
| 50 | .79 | .89 |

Table 2.5: Comparison of photon energy in DET2 with tag energy measurement using a 20% radiator. $E_{tag}$ is the photon energy determined at the RESH detector, $E_{total}$ is the summed photon energy at DET2, and $E_{hot}$ is the energy of the trigger photon only (does not include noninteracting photon energy).

events that can pass our trigger.

The resulting distributions of 'hot' and the 'soft' ($E_\gamma$ < 100GeV) photon energies at our target with a 20% radiator are shown in figure 11. Figure 12 shows the total energy of photons seen at DET2 ($E_{hot} + \sum E_{soft}$) divided by the energy of the radiated photon(s) (computed from the energy loss of the electron in bremsstrahlung = 350GeV-$E_{RESH}$). The spectrum for both 10% and 20% radiators are shown. Table 2.5 lists the results for our nominal running configuration; 20% radiator with MAG1 and MAG2 both on. According to these results approximately $\frac{1}{3}$ of our triggered events have energy loss of more than 10 GeV enroute to our target and 10% lose more that 50GeV. The forward energy contamination is given by the 'soft' spectrum shown in figure 11. The mean contribution is about 12 GeV to the forward energy spectrum but is highly variable.

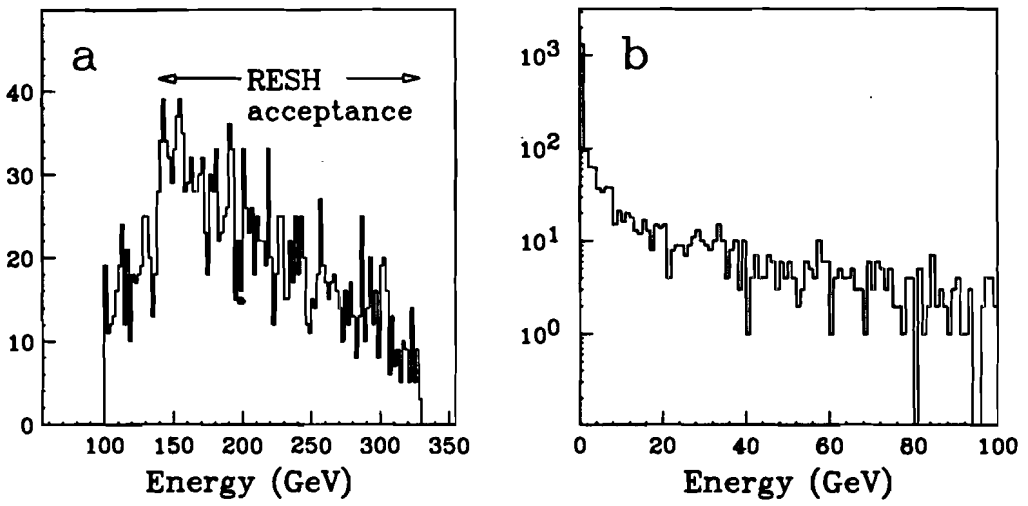


Figure 11: a.) Spectrum of 'hot' photons at DET2 for nominal running configuration (20% radiator and both MAG1 and MAG2 on). b.) Spectrum of 'soft' photons (summed) at DET2.

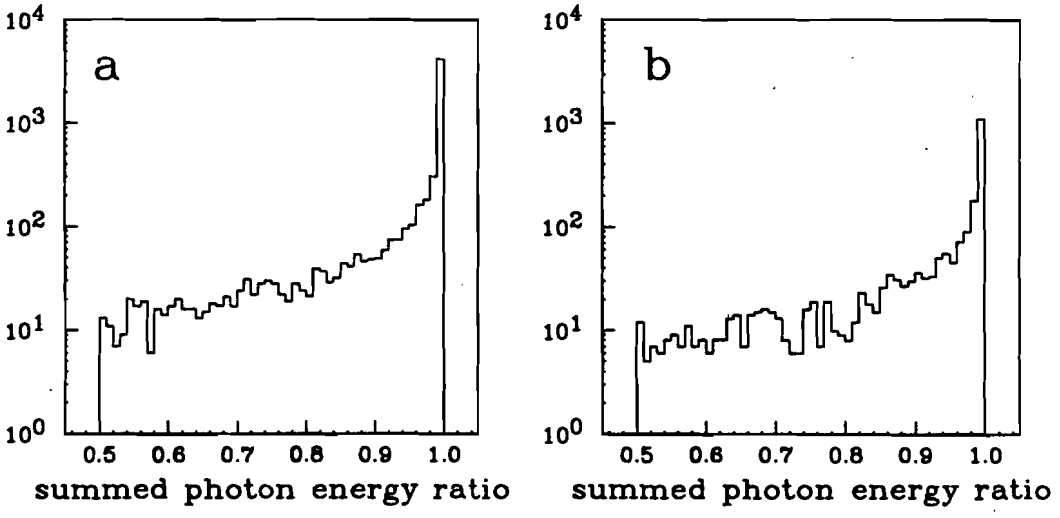


Figure 12: Ratio of total photon energy at DET2 to tagged photon energy (when no charge is present) a.) 10% radiator b.) 20% radiator.

# Chapter 3

# Event Reconstruction and Selection

## 3.1 Data Aquisition

The data were taken using a configuration of several CAMAC crates read out by a Microvax II. This system was adequate for our purposes since we did not require high rate capabilities. The data was written to 9-track tapes (density 6250 bpi) at the rate of about 10Hz. For a given event, the digitized signal words from each device were stored in a variable length data structures called 'banks'. The beginning of each bank was marked by a preassigned data word or series of data words called a 'header flag'. The banks were organized by groups of either detector

system or readout device. In addition, the digitization time for each device was a determining factor in the ordering of the banks. For example, the slowest devices were read out last.

## 3.2 Data Reduction

The data was then processed through the E683 standard analysis code. The first step consisted of unpacking the raw data from the data banks into arrays. Then, depending on the device, further processing was performed as necessary. For example, pedestals were subtracted from raw ADC values and the values were then converted to energies. Also, there was a code for processing the silicon strip hits and outputing the number of tracks, chisquares for each, and the momentum value for single track events. The system allowed for the various trigger types to be unpacked seperately as well as the inter spill record that contained such information as the magnet settings and integrated scaler counts.

## 3.3 Event Selection

Once the physical quantities were reconstructed from the raw data words event selection criteria were applied to eliminate spurious triggered events and to isolate a sample of 'interesting' high $E_t$ events. Care must be taken in the event selection

so as not to introduce biases pertaining to the desired measurement. In our case, the necessary requirements were few and simple.

The spurious data were a consequence of beamline halo muons or MCAL phototube breakdown that fake high $E_t$ as described in detail in section 3 of chapter 2. As mentioned earlier, the hardware vetoes for these spurious events did not completely eliminate them from the data sample. An additional set of offline cuts were applied to eliminate them. These so called 'anti-muon cuts' required that:

1. At least 15 towers have energy greater than 0.5 GeV.

$$N_{towers}(E > 0.5\ GeV) > 15$$

2. The ratio of the larger of the two $E_t$ imbalances, $E_{tdiff}$, to the total $E_t$ be less than 0.7.

$$E_{tdiff}/E_t < 0.7$$

Where $E_{tdiff}$ is the magnitude of the larger of the two differences $E_t(left) - E_t(right)$ or $E_t(top) - E_t(bottom)$. By left or right is meant all towers on either symmetric half of the MCAL that are seperated by a vertical line in the center of the MCAL face (similarly for top and bottom).

The first cut amounts to a crude event minimum multiplicity requirement. The 'muon-like' events had notoriously low multiplicity. The second cut imposes a very loose transverse momentum conservation requirement. These events clearly

had large momentum imbalances. Each was shown to work effectively without introducing significant biases to the data sample [38]. (According to [38], the combined cuts are 99.9 % effective in eliminating the contamination). The 'anti-muon' cuts reduced the data sample by about 12% on average.

It should be noted that these 'muon-like' events had an A-dependent rate. Our trigger required a signal in the post target counter C2 in addition to the high $E_t$ requirement. $e^+e^-$ pairs created by noninteracting photons in our target fufilled the C2 signal requirement for the fake events. The differences in the radiation length fractions for each target were responsible for the A-dependence in the fake event trigger rate. The contaminations ranged from about 6% for $LH_2$ to about 25% for the thick lead target.

Software trigger threshold cuts were applied to sharpen the hardware trigger thresholds. They eliminate the effect of near-threshold inefficiencies in the hardware trigger. The cuts were imposed on each trigger seperately:

$$GLOBAL\ E_t > 8\ \text{GeV}$$

$$TWOHI\ \ E_t > .75\ \text{GeV}$$

The resulting $E_t$ spectrum is shown in figure 13. The low $E_t$ tail results from events that passed only the TWOHI trigger. This data sample will from now on in this thesis be refered to as the 'triggered' data. This means the processed data sample before jetfinding is applied.

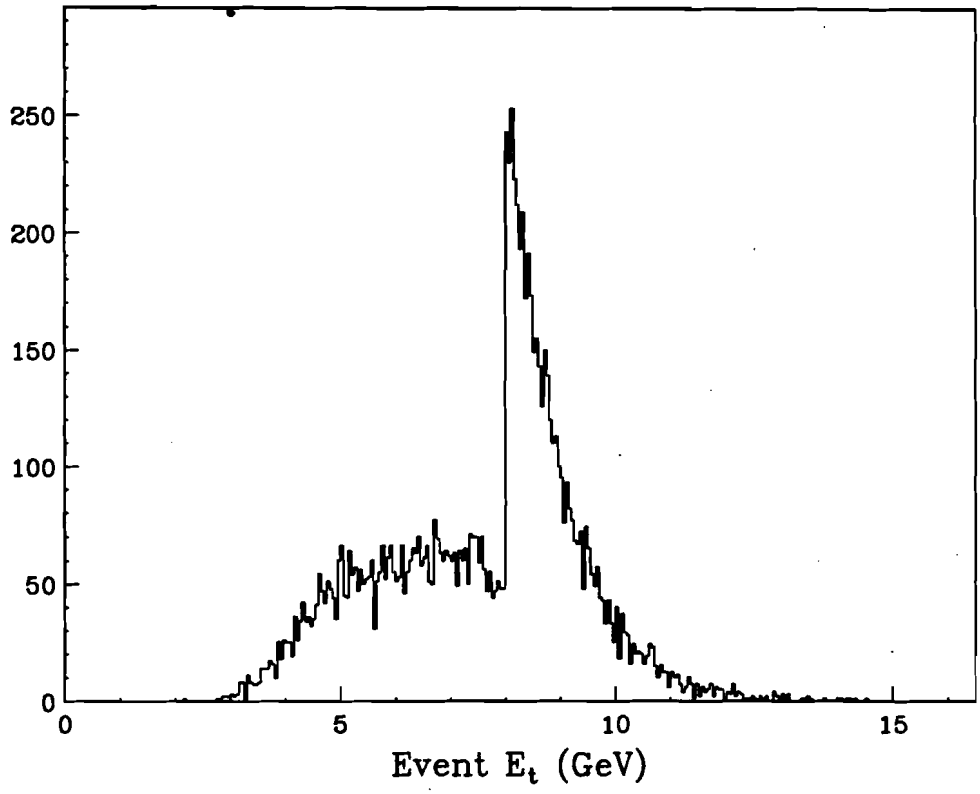


**Figure 13: Triggered $E_t$ spectrum (after event selection)**

It is convenient to introduce a variable that characterizes the 'jettyness' of the data sample. One such variable is called planarity. It is defined by finding the set of orthogonal axes, $(x', y')$, in the transverse plane such that the sum of squares of the momentum components along the $x'$ axis is maximized. Then the planarity is given by:

$$Planarity = \frac{\sum p_x'^2 - \sum p_y'^2}{\sum p_x'^2 + \sum p_y'^2}$$

The more jetlike an event, the closer planarity is to 1. An entirely isotropic event has planarity of 0. Planarity of a di-jet event is affected by both the out-of-planeness of the jet axes as well as the fatness of the jets themselves. Back-to-back jets have higher planarity than out-of-plane jets. In addition, diffuse jets have reduced planarity over highly collimated jets. Di-jet events sitting on an isotropic background will also have reduced planarity from the contribution of the background.

The planarity for each trigger type of the triggered data sample is shown in figure 14. Events triggered by the TWOHI trigger have much higher planarity than the GLOBAL trigger events. This is not suprising since the two hot tower requirement selects events in which each jet's energy is concentrated in a single hot tower. It is also possible, but not as likely, that the two hot trigger towers are within the same jet. Note that the triggers are not mutually exclusive. The two triggers overlap almost completely for events in which two jets are found with

$P_t > 3$ GeV.

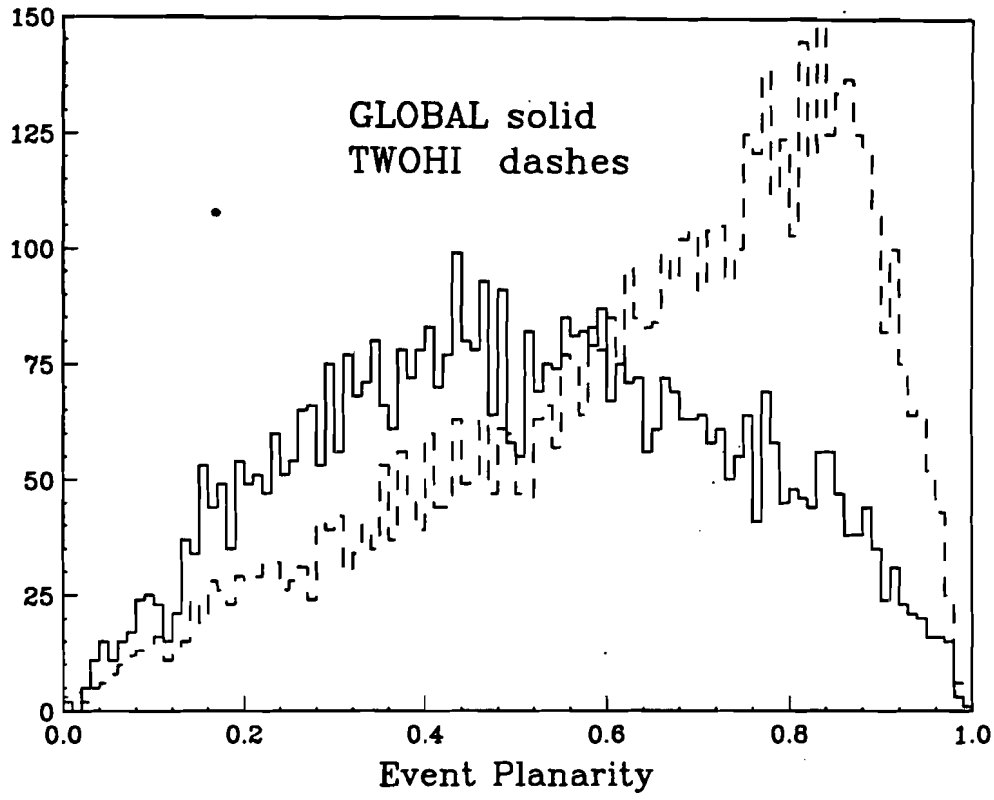


Figure 14: Event planarity of the triggered data sample

## 3.4 Jetfinding

In this section we will present the algorithm used in jetfinding. Experimentally, a jet is not a precisely defined object. The definition of a jet for a given experiment will depend on the detector used and to some extent the kinematic regime of the

experiment. In general Monte Carlo studies are used to decide on a jet definition for a given experiment. The reasons for the choices used here will be discussed in the next chapter where we discuss the study of the algorithm using Monte Carlo generated events and a detector simulation.

The Algorithm is a typical $\eta - \phi$ space cone jetfinder. Variations of this are commonly used to find jets produced from hadron-hadron collisions [39].

## Jet Finding Algorithm

- The 20 hottest MCAL towers with $E_t > .5$ GeV are ordered and tried sequentially as initial jet axes - excluding them as they are included in other jets.

$$PTSEED = .5\ GeV$$

- A cone in $\eta$ - $\phi$ space with radius $R_o = 1.0$ is drawn about the jet axis and a tower is included in the jet if $R < R_o$.

$$where\ \ R = \sqrt{(\eta_i - \eta_{\rm jet})^2 + (\phi_i - \phi_{\rm jet})^2}$$

- $P_t$ of the jet is then given by the total energy in the cone located at the centroid of the energy within the cone.

$$P_t = E_o \sin\theta_o$$

- This defines a new jet axis with which the process is repeated a maximum of 5 times until the $P_t$ of the new axis is less than PTSHFT=.1 GeV from the old one.

$$PTSHFT = .1\ GeV$$

- There is a minimum $P_t$ requirement of 2 GeV on the jet candidate.

$$PTCUT = 2\ GeV$$

- If only one jet is found the remaining towers outside of the found jet are searched taking the maximum of these as a seed in a last ditch attempt to find a jet from the remaining towers.

- If three jets are found the smallest $P_t$ jet is checked to see if its cone overlaps by more than 75% of its energy with either of the others - if so it is combined with the overlapping jet and a new jet is found, otherwise all three are unchanged.

This algorithm was applied to the sample of high $E_t$ triggers discussed above. After applying the jetfinder the data sample consisted of about 43% two jet events, 40% one jet events, and 15% events with no jets found. (three jet events were rare $< 2\%$). The majority of single jet and zero jet events resulted from inefficiencies in finding the low $P_t$ jets. (The efficiency of jetfinding was ascertained from Monte Carlo event studies).

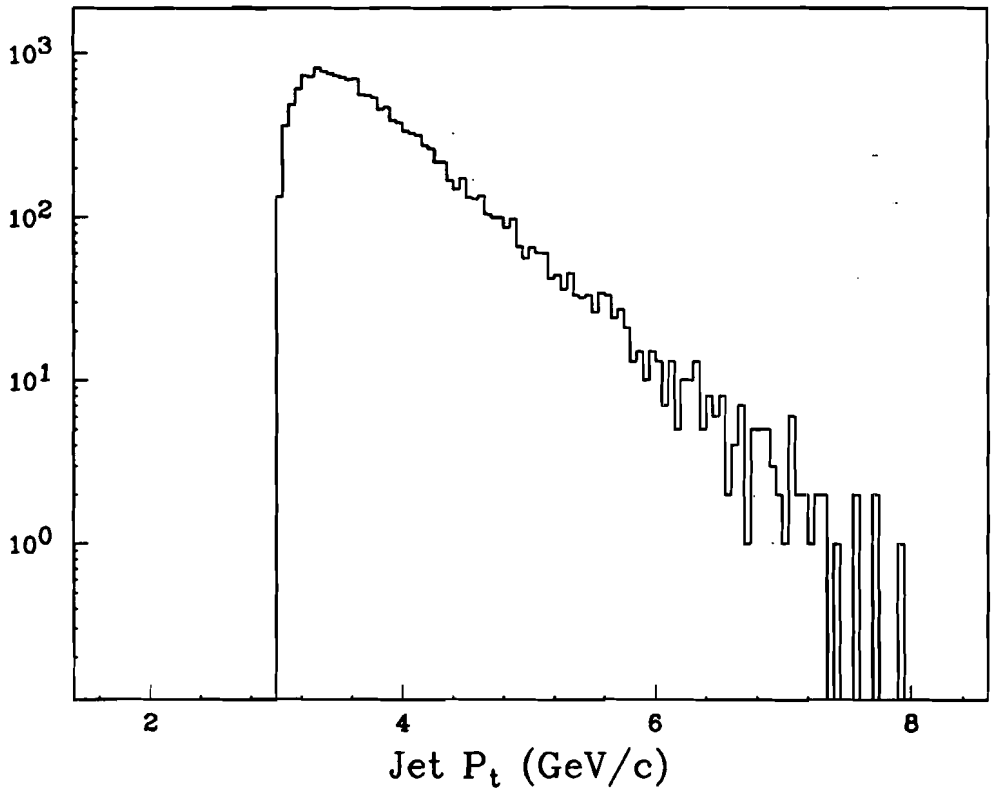


Figure 15: Average jet $P_t$ spectrum

For this analysis we are interested only in the di-jet events. There were two additional cuts imposed on the di-jet sample:

1.) $P_{tjet} > 3$ GeV

2.) $2° < \theta_{jet} < 6°$

The jet average $P_t$ spectrum of the $\gamma p$ data is shown in figure 15. The minimum jet $P_t$ requirement was chosen from Monte Carlo studies which indicate jetfinding was inefficient below about 3 $GeV$. The cut on the polar angle of the jet axis, $\theta$,

(as defined in figure 16), requires containment of the jet in the calorimeter volume. This fiducial volume cut was chosen based on Monte Carlo studies. The boundaries of the cut are approximately drawn in figure 16 (in dots). The minimum jet axis angle is the more sensitive of the two boundaries. There are few events at the outer edge of the MCAL. Also, the 3 GeV $P_t$ minimum cut already restricts the jet containment to some extent.

Shown in figure 17 is the planarity of the di-jet event sample. The planarity of the data sample has increased from a mean of 0.58 for the triggered data to 0.73 after jetfinding.

Figure 18 shows the kinematic correlations found in the di-jet sample. Figure 18a shows that the difference in azimuth of the two found jets, $\Delta\phi$, is peaked at 180°. (The azimuthal angle, $\phi$ is defined in figure 16). Thus the di-jets are coplanar on average. Figure 18b shows that the jets balance in $P_t$ on average. Where $\Delta P_t$ is the absolute value of the $P_t$ difference of the two found jets.

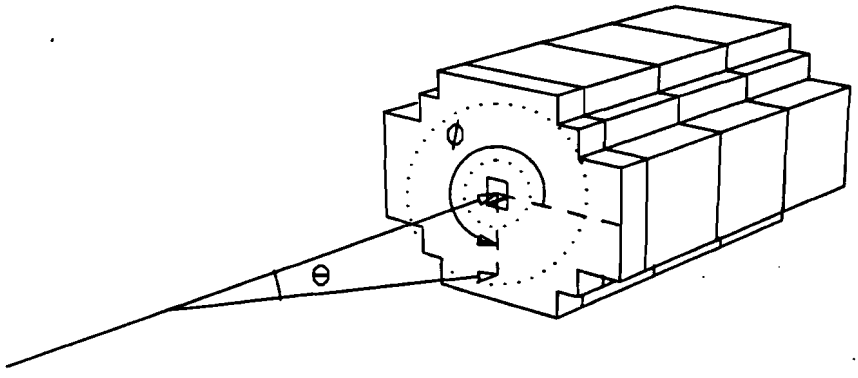


Figure 16: E683 Coordinate System (fiducial volume cuts shown approximately in dots).

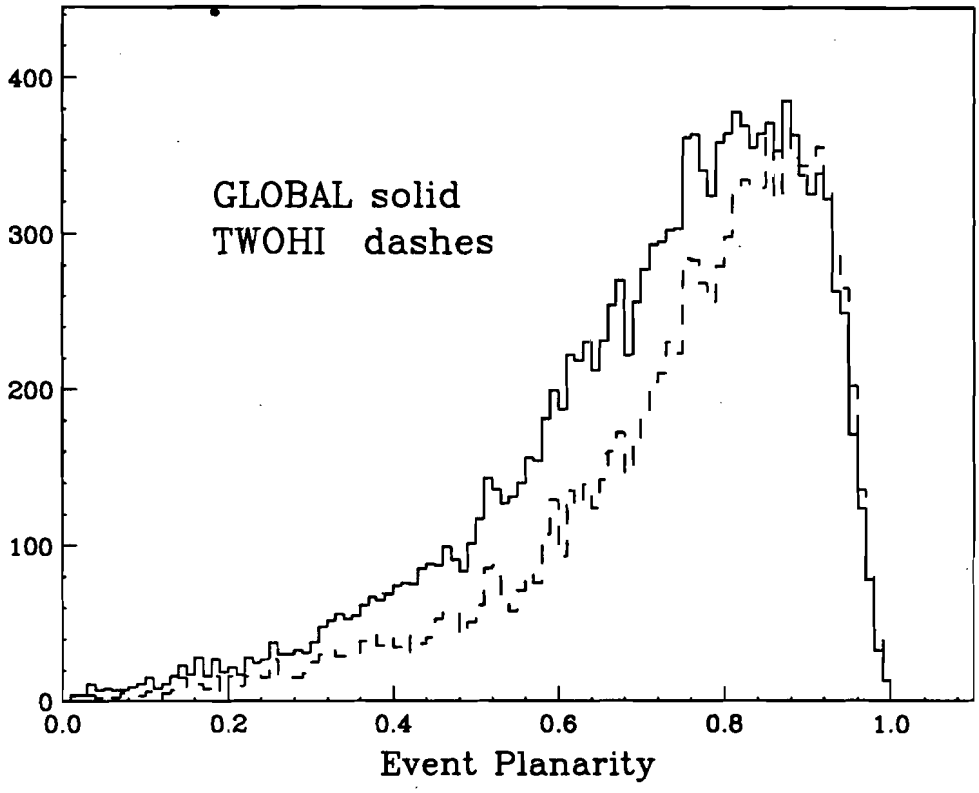


**Figure 17: Planarity of di-jet event sample.**

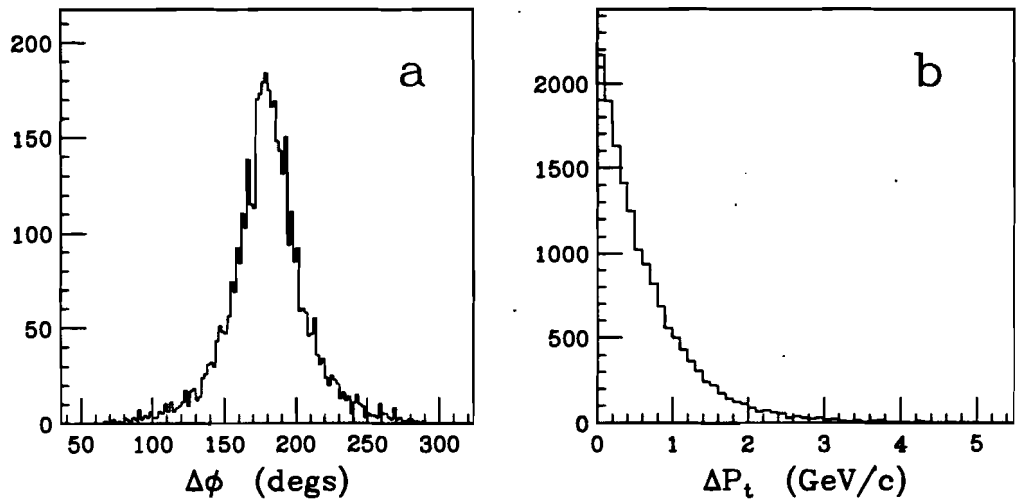


Figure 18: a.) Azimuthal correlation of the found jets b.) $P_t$ balance of found jets $|\Delta P_t|$

# Chapter 4

# Monte Carlo Studies

## 4.1 Generators

Monte Carlo events generators were developed as a tool to aid in making predictions and interpreting observed phenomema in terms of fundamental underlying theory. They are especially needed at high energies where particle production is increasingly complex. They have traditionally been used to study the effects of detector response, resolution, and acceptance on the desired measurement. That is, they can be used to determine how well a quantity can be measured with a given detector system and also be used to make corrections to the measurement if possible.

The two industry standard Monte Carlo event simulators, PYTHIA[40] and

HERWIG[41], factorize the process of event generation into three steps:

$$hard\ QCD \oplus parton\ showering \oplus fragmentation.$$

The major difference between HERWIG and PYTHIA is in the fragmentation scheme used. The hard subprocesses themselves are constrained by QCD. The two codes may also use slightly different structure functions, evolution scales, and cutoffs but these are minor differences.

Table 4.1 summarizes the main differences in the Monte Carlo generators studied. The fragmentation models IF (=independent fragmentation), SF (=string fragmentation), and CF (=cluster fragmentation) that are available for each generator are shown. [1] LUCIFER and TWISTER codes do not include parton showering but instead tune the fragmentation process to reproduce the observed distributions. The $Q^2$ dependence, a feature easily incorporated into parton showering models, can not be reproduced by a single tuning of fragmentation. For this reason these models have been superseded.

The event generators have some adjustable parameters to be chosen by the user. The differential cross section is divergent as $p_\perp \to 0$. A lower cutoff value, QTMIN, must be chosen to avoid the divergence. There is some danger in choosing it too small since the leading order treatment breaks down at small momentum

[1] PYTHIA has the IF option but it has not been retuned after gluon radiation was included and therefore will not be used.

| code | Fragmentation model(s) | Parton Showering | Comments | Reference |
|---|---|---|---|---|
| PYTHIA 5.6 | SF,IF | yes | all processes | [40] |
| HERWIG 5.5 | CF | yes | all processes | [41] |
| TWISTER | SF,IF | no | VDM, anomalous $\gamma p$ and $\pi p$ | [43] |
| LUCIFER | SF,IF | no | direct coupling $\gamma p$ only | [42] |

Table 4.1: Monte Carlo event generators studied.

transfer. For our purposes a QTMIN of 2 GeV is chosen. It appears from studies of this cutoff (down to 1.0 was studied) that events originating from lower momentum transfer values rarely pass our trigger in any case. For all other parameters default values were used in these studies, unless otherwise specified.

## 4.2 Detector Simulator

The Monte Carlo events can then be studied in the context of our particular detector by using a code to simulate the MCAL detector response and acceptance. The code was developed by M. Corcoran [44]. The inputs are the momentum vectors and energies for each final state particle with a flag indicating particles which shower hadronically. The outputs are the energy in each calorimeter tower for each of the four layers, the energy that was deposited into the MCAL hole, and the energy that missed the outer edge of the MCAL. Specifically, the following

features are incorporated:

- The longitudinal shower developement and resolution functions for electromagnetic and hadronic energy loss are based on calibration data measurements.

- Lateral shower spreading into neighboring modules is modeled based on a gaussian shower spreading algorithm.

- Spillover energy loss through the MCAL hole into BCAL is modeled based on a parameterization of our calibration data.

From this information tower sums are formed as in the data. The trigger cuts are then applied for both trigger types:

$$1.)\ GLOBAL > 8\ Gev$$

$$2.)\ TWOHI > .75\ Gev$$

The jetfinder is applied to this set of generated triggered events. The same two additional cuts that were applied to the jet data, $P_t > 3$ GeV and $2^\circ < \theta < 6^\circ$, were also applied to the Monte Carlo events. The results can then be compared with those of the data distributions.

## 4.3 Monte Carlo Comparison with Data

Figure 19 shows the comparision of some sensitive data distributions with the Monte Carlo simulation result. All of the Monte Carlo simulation results discussed will be a mixture of 30% direct coupling photon processes with 70% extended photon processes. The relative proportion of the processes generated was chosen based on the predictions for the integrated total cross section for each process with parton $P_t$ greater than 1.5 GeV. In the case of the comparison shown in figure 19 the events were generated using LUCIFER for the direct coupling processes and and TWISTER for the extended photon processes [2]. The independent fragmentation option was also used in this case. A mixture of three beam energies was used for the comparison; 30% at 200 GeV, 40% 250 at GeV, and 30% at 300 GeV.

The total event $E_t$ in the MCAL, event planarity, and average jet $P_t$ distributions are shown. The Monte Carlo reproduces the shapes of these sensitive distributions adequately. The $E_t$ flow distribution for calorimeter towers is shown in figure 20. The '$E_t$ flow' is defined as the azimuthal opening angle of each tower measured from the axis of the hotter jet (plotted on the x-axis) weighted by the $E_t$ of that tower and normalized by the number of events. This distribution shows

[2] 20% VDM photon with switch IPY(15)=0 and 50% anomalous photon with IPY(15)=2.

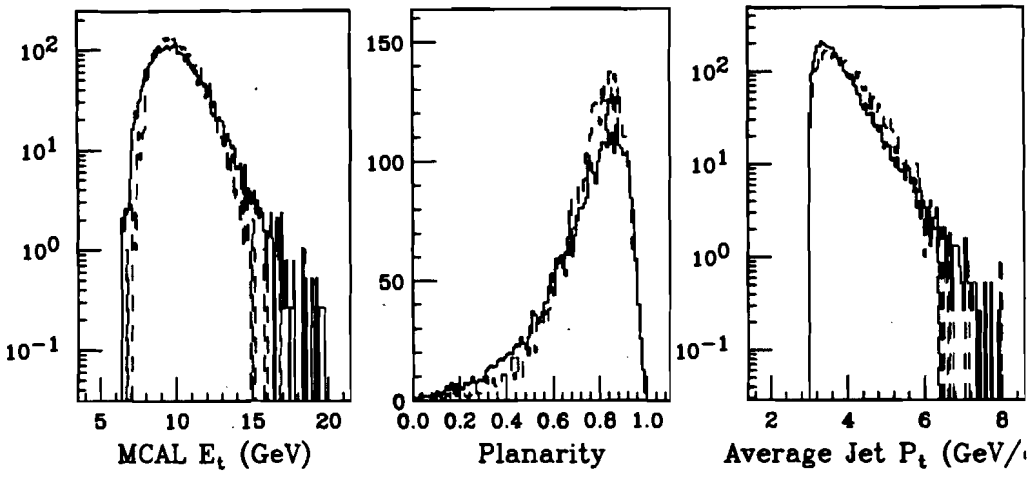


Figure 19: Comparison of jet events with Monte Carlo a.) MCAL $E_t$, b.) planarity c.) average jet $P_t$. (solid lines are data, dashed are Monte Carlo)

the jet structures near $0^{circ}$ and $180^{circ}$ sitting on a flat background from the soft underlying event.

A comparison with the PYTHIA(5.6) (string fragmentation option) results indicate that the jets produced by string fragmentation are slightly more planar than jets measured. The planarity of string fragmentation jet events is too high and there is too little $E_t$ outside of the jet cone to model our data. However, the agreement is only slightly worse as a whole. HERWIG gives distributions that are roughly in agreement with the PYTHIA results. [3]

[3]Herwig default values include an underlying event enhancement that has been tuned using $pp$ collisions. There is no indication that such an enhancement is needed in $\gamma p$ data. For the studies in this thesis the enhancement is turned off for all $\gamma p$ comparisons.

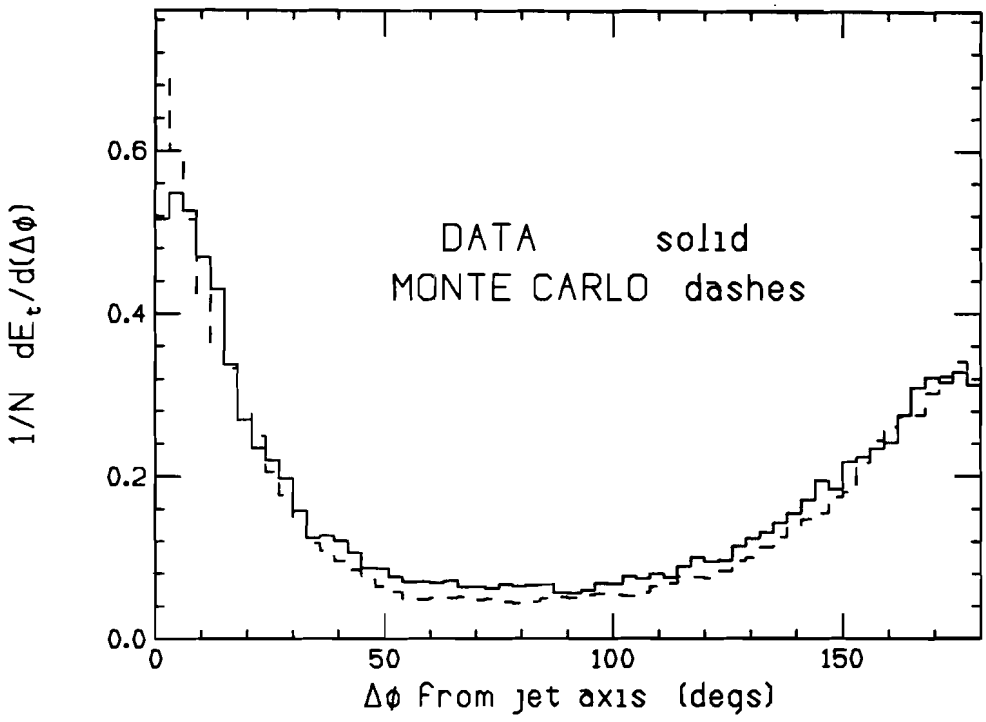


**Figure 20:** $E_t$ **flow comparison with Monte Carlo**

## 4.4 Jetfinding Studies

The main purpose for implementing the simulation was to use it to study our ability to correctly find and reconstruct di-jet events. For the rest of this chapter only results from the LUCIFER/TWISTER Monte Carlo that was compared with the data in figure 19 will be discussed. Based on Monte Carlo results our efficiency of jetfinding was diminished below $P_t$'s of about 3 GeV. In general, these events did not meet the hot seed requirement in the MCAL of 0.5 GeV for one or both of the jets. Jetfinding efficiency was less than 20% for di-jet events with average jet $P_t$ below 3 GeV. Furthermore, reconstructed $P_t$ of these jets were less correlated with the 'true' jet $P_t$'s than the higher $P_t$ sample. These two results were the basis of the minimum jet $P_t$ cut of 3 GeV chosen in our data sample.

Here some statements must be made about reconstructing parton kinematics. In this thesis the 'true' jet is defined as the particles that originated from the parent parton that fragmented. This quantity is only defined in the independent fragmentation concept. Relating the found jet kinematics back to parton level variables requires choosing a fragmentation model. The mapping to partons is very different for each model presently available. Properties of the 'true' jet are measureable. Simulations are only required to reproduce the measured properties at the 'true' jet level. No attempt will be made to relate jet quantities back to the parton level. We will only make comparisons of found jet quantities to the 'true'

jet level.

The momentum vector of the 'true' jet is defined by the vector sum of the momenta of the particles in the jet. The scaler sum of the particles' energies defines the energy of the 'true' jet. The jet defined in this way has a non-zero mass from $E^2 = p^2 + m^2$. The jet mass comes about from the components of momentum transverse to the jet's axis of particles within the jet.

The jetfinder cone size of $R = 1.0$ in $\eta\phi$ space, (a standard choice for fixed target experiments), was studied by a comparison with the vector sum variables. It is generally considered most important to get the jet's $P_t$ right. In our case, the vector sum $P_t$ of the jets agreed on average with the found jet $P_t$'s for a cone size of 1.0. The difference distribution is shown in figure 21a.

The dashed curve is the same distribution with the effect of calorimetry removed. That is, the jetfinding for the dashed curve was performed on particles themselves and not calorimeter towers. (It also includes the same acceptance as the MCAL for comparison). This distribution has a mean of $-0.17 \pm .01$ GeV. The jetfinder, acting on particles, finds the jet $P_t$ too large by about this amount on average. The spike at zero difference occurs for events in which the jetfinder reconstructs the true jet $P_t$ perfectly.

The difference in the mean of the two distributions shows the effect of the assignment of an electromagnetic energy loss calibration factor for layers $A'$ and

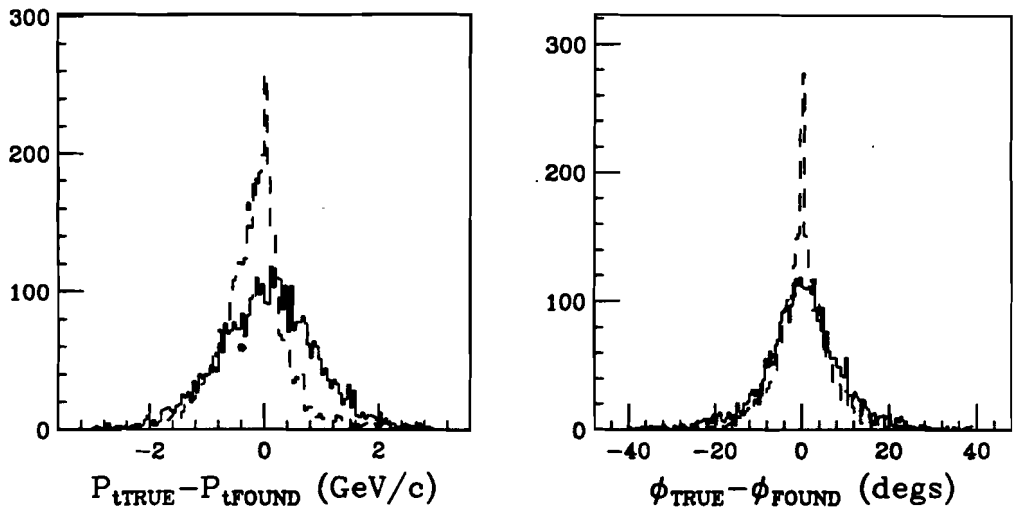


Figure 21: Jetfinding studies in $P_t$ and $\phi$. a.) difference distribution in $P_t$ of the true jet minus the found jet. (solid lines are for calorimeter jets and dashed are for particle jets). b.) difference distribution in $\phi$.

$A$ as discussed in Chapter 2. The energy scale, (and similarly the jet $P_t$ scale), is systematically underestimated due to this effect. The effect of the cone size in overestimating the $P_t$ of the particle jet and the energy scale underestimating it appear to approximately cancel. Thus the cone size chosen appears to get the $P_t$ right on average.

Calorimetry also has a large effect on the width of this distribution. The distribution has an RMS width of 0.8 GeV. The next section will discuss a method to correct for this width and the width due to particle inclusion errors in the jet cone.

Shown in figure 21b is the difference distribution for the jet $\phi$ compared with

vector sum $\phi$ for each jetfinder. The jetfinder also gets the $\phi$ angle correct on average. The RMS of this distribution is about 7°. Calorimetry adds only a small contribution to the width of the difference spectrum as can be seen by the comparison with the particle based jetfinder difference spectrum (in dashes).

The jet's polar angle, $\theta$, and energy are both systematically off from those of the vector sum. They can be adjusted to correct for this offset if necessary. They are not used in this analysis and will not be discussed further here.

## 4.5 Jetfinding Correction

The jetfinding correction attempts to remove contributions to a jet quantity that result from the detector and the jetfinding method. For example, the calorimetry adds a width to the jet measurements due to the energy resolution, the tower position granularity (the energy in each tower is assumed localized at the center), lateral shower spreading and energy leakage out of the detector. The cone jetfinder may fail to include some true jet particles and include others that did not belong to the jet being measured. For our purposes both classes of jetfinding errors will be lumped together and considered as the contribution due to our calorimeter based jetfinding. A method to correct for these effects will be discussed briefly here and in more detail in the next chapter.

The flow diagram in figure 22 shows the method schematically. Using the

Monte Carlo discussed above with the independent fragmentation option the vector sum quantities of the true jet of particles are constructed for each event. We then simulate the event in our detector and apply the jetfinding algorithm to the tower as in our data analysis. Then by comparing the resulting jet distributions with the true jet vector sum distributions a correction for the ensemble distribution can be obtained. Note that the definition of a jetfinding correction for this thesis will be a correction to the ensemble distribution. The correction does not have meaning on an event by event basis.

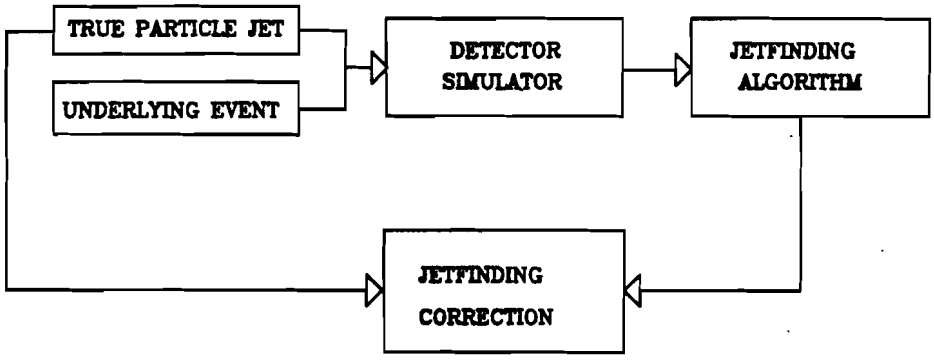


Figure 22: Method for determining the jetfinding correction.

This method relies on the event generator to model the true particle jets and the underlying event from remnant jets both of which contribute to the particle inclusion errors. In addition, we must be convinced that the MCAL simulator does a resonable job of modeling the detector behavior. Some confidence can be

gained of this from the data/Monte Carlo comparison shown earlier for our photon data. This turns out not to be the case for our pion data for which we had to model additional contributions and include them in the Monte Carlo by hand. This will be discussed in the next chapter.

The jetfinding contributions are assumed uncorrelated to the jet quantity measured (an assumption that is not unreasonable for the distributions we will study). The jetfinding correction is obtained by the quadrature subtraction of the width of the true jet distribution from that of the found jet distribution. This correction is then subtracted from the width of the data distribution in quadrature.

# Chapter 5

# Results and Discussion

## 5.1 Differences in $\gamma p$ and $\pi p$ Jet Events

E683 took about 10% of its data with a broad momentum spectrum $\pi^-$ beam. The mean energy of the pion beam was chosen to roughly match that of the photon beam ($< \sqrt{s} > \sim$ 21.5 GeV). The $\pi$ momentum spectrum is shown in figure 23. Since the same detector and beamline were used for both data samples the systematic errors in comparing results from the two different beam flavors should be minimized.

Significant differences were seen between pion and photon beam events for both the triggered data and the jet data. For example the pion data was much less planar than the photon data for the same found jet $P_t$ range. The differences

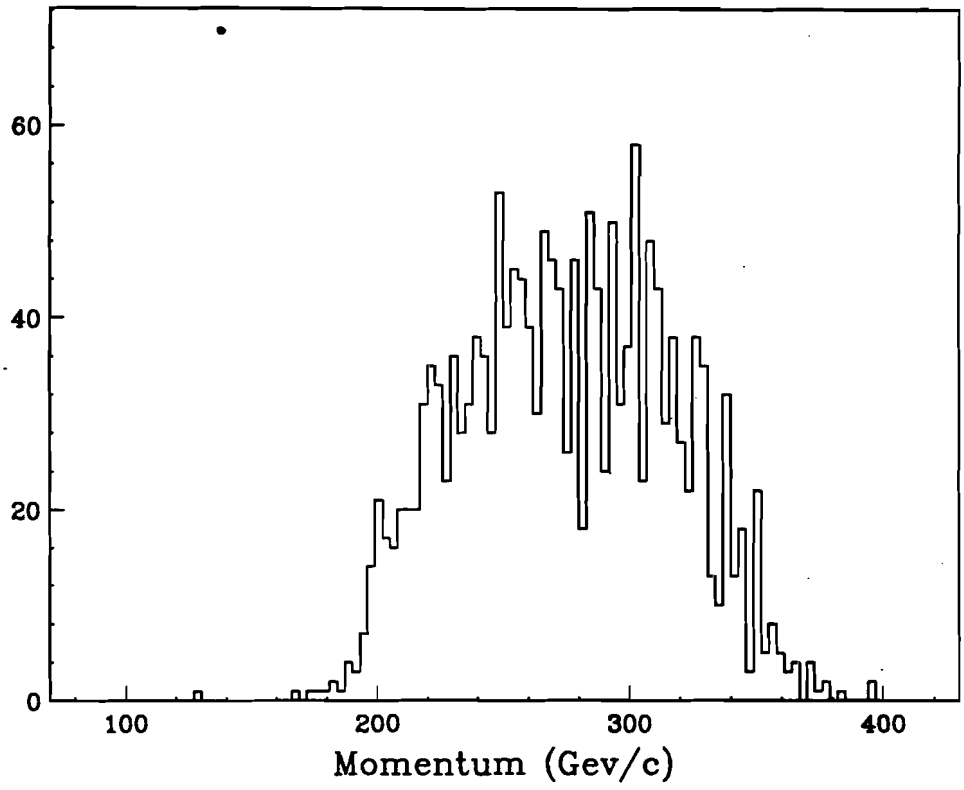


**Figure 23: Pion beam momentum spectrum selected by di-jet events**

seen persisted through the entire range of $P_t$ measured. This difference is shown in figure 24 which plots the mean planarity as a function of average jet $P_t$ for $\gamma p$ and $\pi p$ .

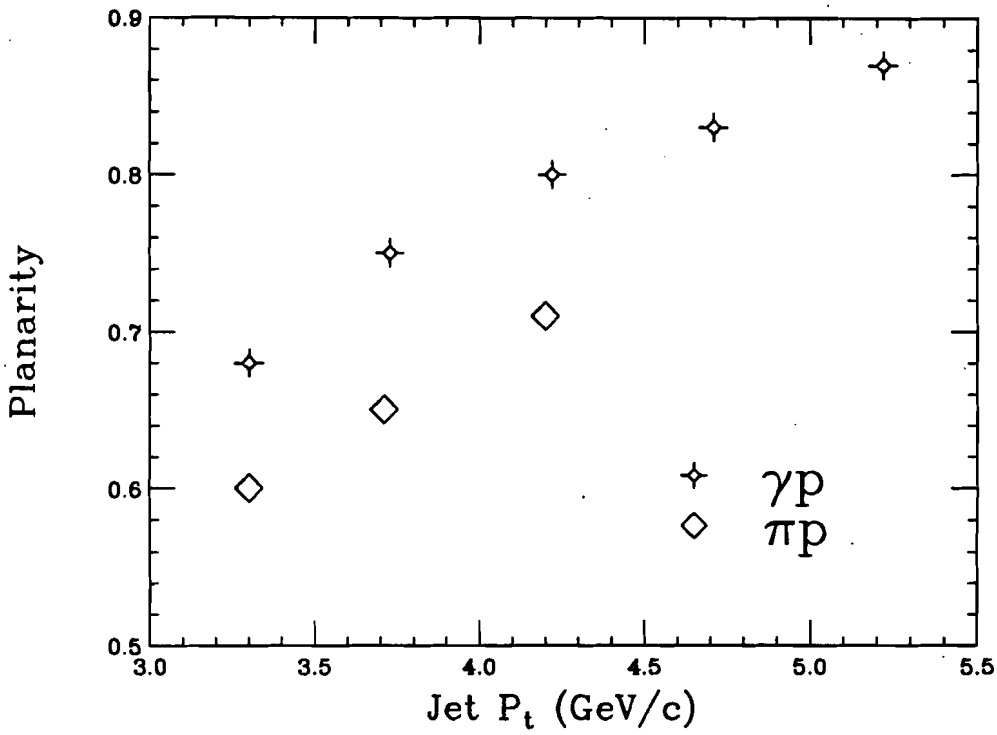


Figure 24: Average jet $P_t$ dependence of planarity (error bars are smaller than symbol dimensions).

As mentioned earlier, the planarity variable is affected by several aspects of the event structure including the jet shapes, out-of-planeness of the jet axes, and the distribution of the non-jet background event. To look directly at the jet out-of-planeness we use the variable, $\Delta\phi$, which is defined as the angle in the transverse

plane between the two jet axes:

$$\Delta\phi = \phi_1 - \phi_2 \qquad for\ \phi_1 > \phi_2$$

$$and \quad \Delta\phi = \phi_1 - \phi_2 + 360^\circ \quad for\ \phi_1 < \phi_2$$

Figure 25 shows a comparison of $\Delta\phi$ for the $\gamma p$ and the $\pi p$ data normalized to the same area. Both distributions are peaked at 180° but the $\pi p$ distribution is much broader than the $\gamma p$ distribution. The RMS width of the distribution is $\sim 37^\circ$ for the $\pi p$ data and only $\sim 27^\circ$ for the $\gamma p$ data.

We expect some differences in these distributions. Both parton primordial Fermi motion and soft gluon radiation from initial and final state partons will contribute to the out-of-planeness of the event. These contributions are expected to be different in $\gamma p$ and $\pi p$ interactions. The initial state contributions may be larger in the pion beam case, as discussed in Chapter 1 (section 4). In addition, the final state leading order processes in the two cases may consist of different proportions of quarks and gluons which have different gluon radiation contributions. The expected size of the various contributions can be investigated with Monte Carlo simulations.

As mentioned earlier, the LUND Monte Carlo code, 'PYTHIA', has an option to include both gluon radiation and intrinsic parton $k_t$ contributions. Shown in figure 26 are the individual contributions to $\Delta\phi$ at the parton level as predicted by PYTHIA. In the absence of all of the above effects the partons emerge from

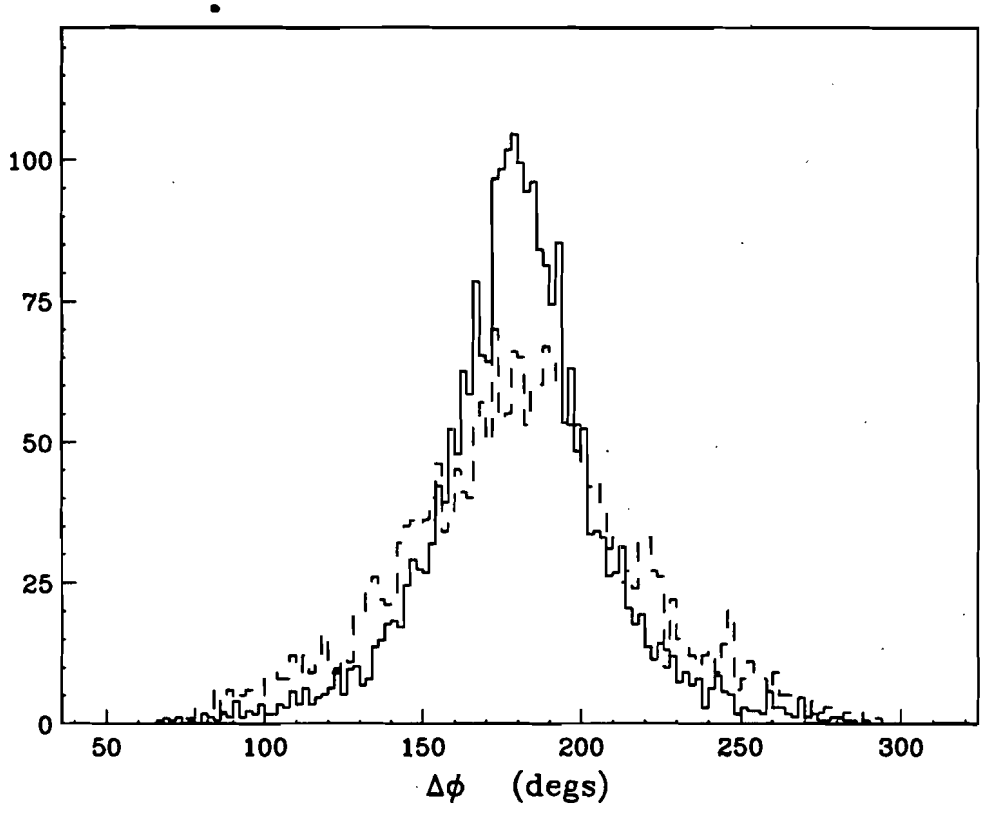


Figure 25: $\Delta\phi$ spectrum for $\gamma p$ (solid) and $\pi p$ (dashes) normalized to the same area.

the hard scatter back-to-back. In this case, $\Delta\phi$ would have $\delta$-function distribution at 180°. This is represented by the narrow spike in frame (a) of the figure. If a gaussian smearing due to intrinsic motion of partons within the nucleon is included the distribution takes on a width as shown in frame (b). The primordial $k_t$ distribution used in PYTHIA gives the partons an x and y component of momentum, $(k_x, k_y)$, each distributed as a Gaussian with width .31 GeV and tails that cut off at 2 GeV from the mean. (This results in a width of 0.44 GeV for the two components in quadrature which is an estimate for the parton $k_t$ inside a nucleon based on the uncertianty principle). The contributions expected for gluon radiation are shown in the next frame, (c). When a parton radiates a gluon, its direction can be perturbed by a large amount which results in the long tails of the distribution.

The differences predicted at the parton level for $\pi p$ vs $\gamma p$ need not be preserved at the found jet level. For example, the effects of gluon radiation may be diminished by inclusion of radiated gluons in the jet cone. The difference in the RMS width of the $\Delta\phi$ distributions for $\pi p$ vs $\gamma p$ is on the order of 12° when subtracted in quadrature at the parton level. The Monte Carlo predicts about 9° difference at the found jet level. Clearly the difference seen in the measured distributions at the particle jet level is much larger ($\sim 25°$). Also, the $\Delta\phi$ distributions at the found jet level shown in figure 25 are much broader than those at the parton level.

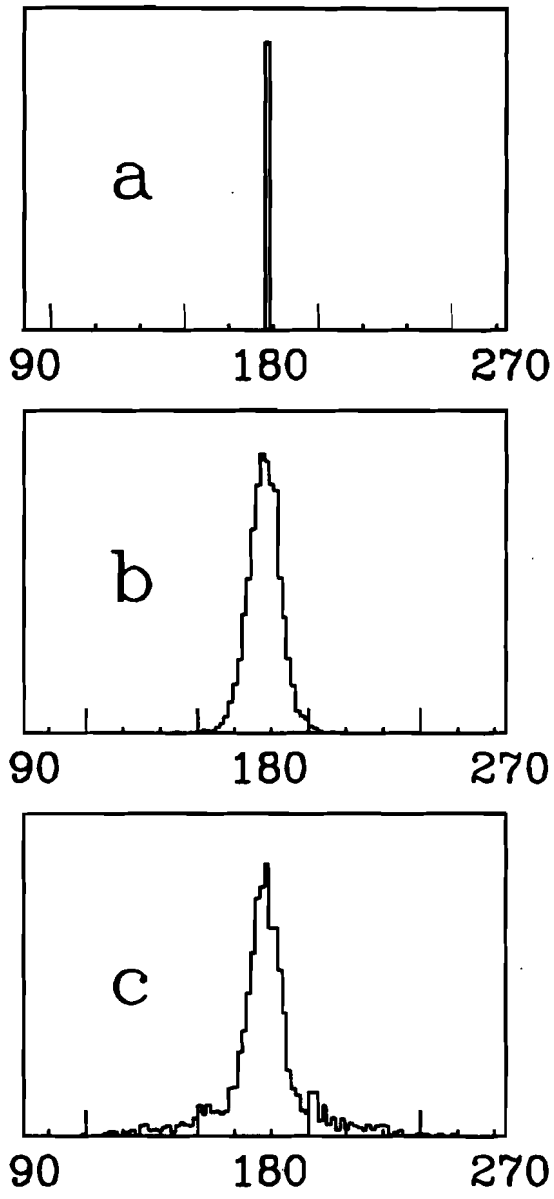


Figure 26: Contributions to $\Delta\phi$ of partons for $\pi p$ a.) kinematic b.) intrinsic $k_t$ c.) gluon radiation.

As discussed in the previous chapter the calorimetry and jetfinding are responsible for the additional width.

As mentioned earlier in Section 1.3, the amount of gluon radiation emitted by a virtual parton depends on its maximum virtuality which is characterized by the momentum transfer scale of the reaction, $Q^2$. Thus QCD predicts that the gluon radiation contributions should scale with $Q^2$. For us, the $Q^2$ scale can be characterized by the average transverse momentum squared of outgoing partons.

The variable, $\Delta\phi$ , has a simple kinematic dependence on transverse momentum. For a fixed out-of-plane component of transverse momentum, $\Delta\phi$ increases with decreasing $|P_t|$. We can remove this kinematic dependence by looking directly at the out-of-plane component of the transverse momentum, $K_{t\phi}$ .

Using the plane defined by the beam direction and the hotter of the two jet's momentum vector, the out-of-plane component of the transverse momentum, $K_{t\phi}$ , is defined as:

$$K_{t\phi} = P_t \sin(\Delta\phi),$$

where $P_t$ is the average jet transverse momentum for the event and $\Delta\phi$ is the azimuthal opening angle between the two jets as defined above. For a Gaussianly distributed $K_{t\phi}$ distribution the single component RMS $K_t$ is given by

$$< K_t^2 >= \frac{\pi}{2} < K_{t\phi} >^2$$

Figure 27a shows $K_{t\phi}$ as a function of average jet $P_t$ for both $\pi p$ and $\gamma p$ .

$K_{t\phi}$ appears not to vary much over our range of $P_t$'s. Figure 27b shows the predictions of PYTHIA Monte Carlo for the same curve. Monte Carlo results show a similar flat dependence over our small range of $P_t$'s. PYTHIA does not predict the large offset in $K_{t\phi}$ in $\pi p$ as compared with $\gamma p$ that we see in our data.

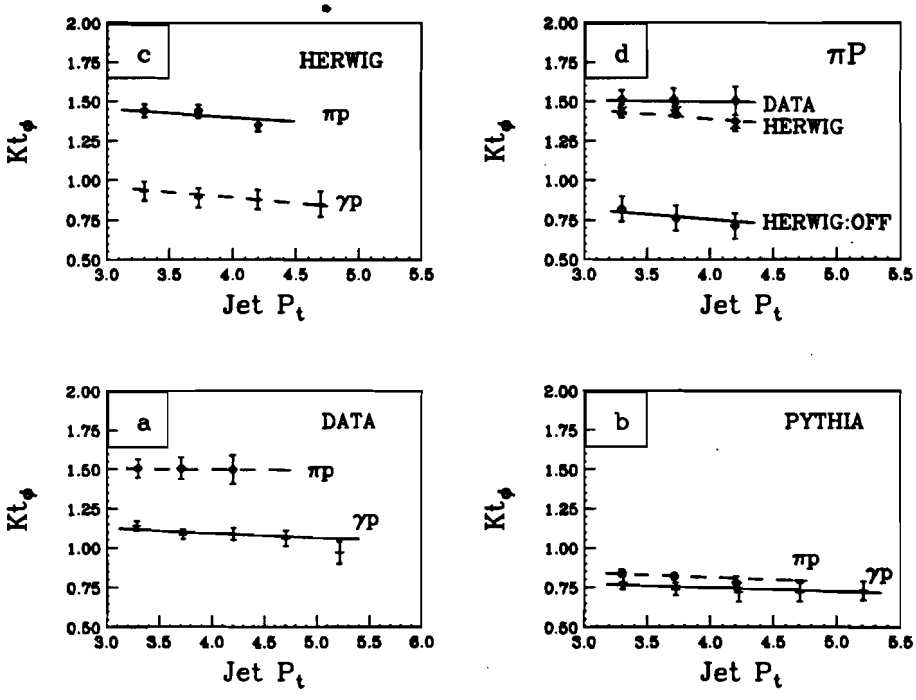


Figure 27: $K_{t\phi}$ vs $P_t$ for $\gamma p$ and $\pi p$ a.) data b.) PYTHIA c.) HERWIG d.) effect of turning off the underlying event enhancement in HERWIG $\pi p$ .

HERWIG Monte Carlo does predicts a large difference between $\pi p$ and $\gamma p$ - similar to the difference we see in the data. Figure 27c shows the HERWIG predictions. The reason for HERWIG's agreement with our pion data is its parameterization of the enhanced soft underlying event distribution in $\pi p$ collisions.

In $\pi p$ collisions, the event topology is different than for direct coupling processes in $\gamma p$ collisions. In $\pi p$ collisions one of the partons in the beam interacts with a target parton leaving behind a remnant in each the beam and the target which produce a beam and a target jet. In the case of the direct coupling photon the beam jet is absent. Thus there is more non-jet $E_t$ present in the $\pi p$ collisions from the remnant jets that can interfere with jetfinding. The additional particles under the jet cone from the underlying event can artificially increase the measured jet $P_t$ and add uncertainty to the jet angular determinations. Figure 27d shows the effect on $< K_{t\phi} >$ of turning off this additional soft underlying event contribution in $\pi p$ .

The authors of HERWIG have found that the data can be well modeled by the superposition of hard scatter and a minimum bias type collision of remnant jet particles [45]. A minimum bias event is one that makes no requirements (or minimal requirements) on the $E_t$ of the system. In a minimum bias collision the beam and target collide with no requirement on a hard interaction having taken place. This is thought to be a reasonable model for the collision of the remnant system in a hard-scatter event. The interaction and fragmentation of the remnant system is refered to as the 'underlying event'. The parameterization of the underlying event that HERWIG uses is based on measurements of experiment UA5 minimum bias data[46]. The parameterization is scaled by the center of

mass energy in HERWIG. The multiplicity of the underyling event is required to match a value preselected from the scaled down UA5 distribution. Momenta of the clusters are then generated according to longitudinal phase-space with transverse momentum constrained to obey an exponential distribution.

We have found that the LUND Monte Carlos do not model our underlying event adequately. A mechanism to enhance the multiplicity in the underlying event collision is available in the latest version of PYTHIA [47]. The so called 'multiple interactions model' allows for the remnants to have an increased probability for multiple hard interactions. We saw no improvement from adding this mechanism in our simulations.

Additional evidence that the underlying event is much larger in our pion data can be seen in figure 28a where the non-jet $E_t$, (the $E_t$ outside of the jet cone), is plotted as a function of average jet $P_t$. The non-jet $E_t$ for $\pi p$ is about 25% higher than that for $\gamma p$ . The $E_t$ flow shown for both $\pi p$ and $\gamma p$ data in figure 28b has differences as well. The underlying event level, seen in the $E_t$ flow plot as the flat region between the two jet peaks, is clearly larger in our $\pi p$ data.

Comparisons between the TWISTER and HERWIG $\pi p$ results demonstrate that the HERWIG parameterization of the underlying event in $\pi p$ is a better model of our data. Figure 29 shows the comparisons for the non-jet $E_t$ dependence on $P_t$ and the $E_t$ flow for each Monte Carlo.

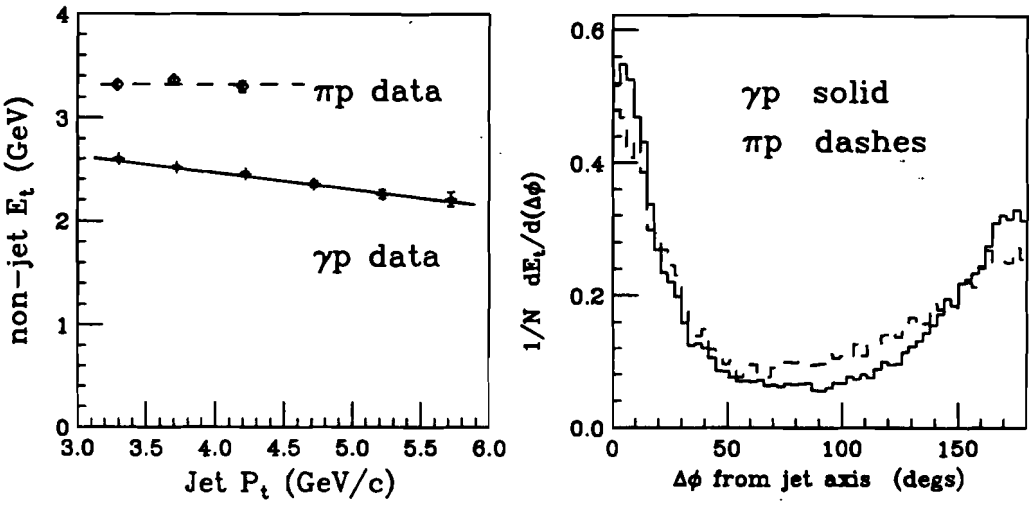


Figure 28: Underlying event comparison $\pi p$ and $\gamma p$ data.a.) Non-jet $E_t$ b.) $E_t$ flow

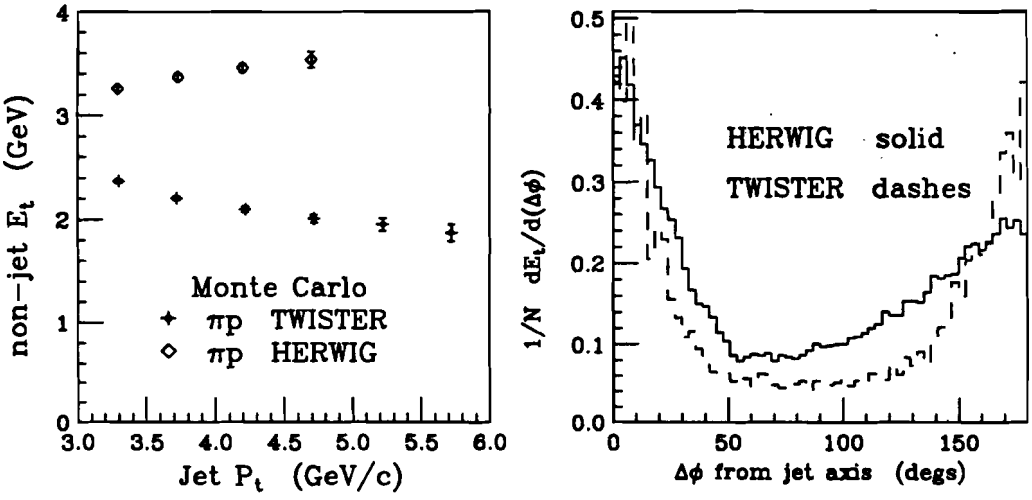


Figure 29: HERWIG Monte Carlo results compared with TWISTER for $\pi p$ a.) non-jet $E_t$, b.) $E_t$ flow

In Conclusion, we have seen that our $\pi p$ vs $\gamma p$ differences can be accounted for by a difference in the non-jet $E_t$ background in the two cases. Physically, this background can come about from the soft underlying event collision between beam and target remnants in $\pi p$ . We expect this contribution to be smaller for $\gamma p$ if direct coupling processes dominate since the beam jet is absent in that case.

## 5.2 A-dependence of $K_{t\phi}$

A strong nuclear dependence is seen in the variable $K_{t\phi}$ both for $\gamma A$ and $\pi A$ interactions. Figure 30 shows $K_{t\phi}$ plotted as a function of atomic weight, A, for both beam types. There are no additional cuts or corrections included here beyond those discussed in chapter 3. It should be noted that the effect seen here is due to a A-dependence in $\Delta\phi$ . The average jet $P_t$ did not vary with A. Figure 31 shows $\Delta\phi$ itself plotted as a function of A. $K_{t\phi}$ will be used to study the A-dependence so that the kinematic $P_t$ dependence of $\Delta\phi$ is removed (as discussed above).

A fraction of about 10-20%, depending on the target, of reconstructed jet events come from other than the target material itself. These events probably come from interactions in the trigger counter C2 or the target tent. The contribution from these events to $K_{t\phi}$ is removed for each target by normalizing the empty target $K_{t\phi}$ distribution to the same flux as contributed to the target distribution and subtracting it bin by bin from the target distribution. The flux used to nor-

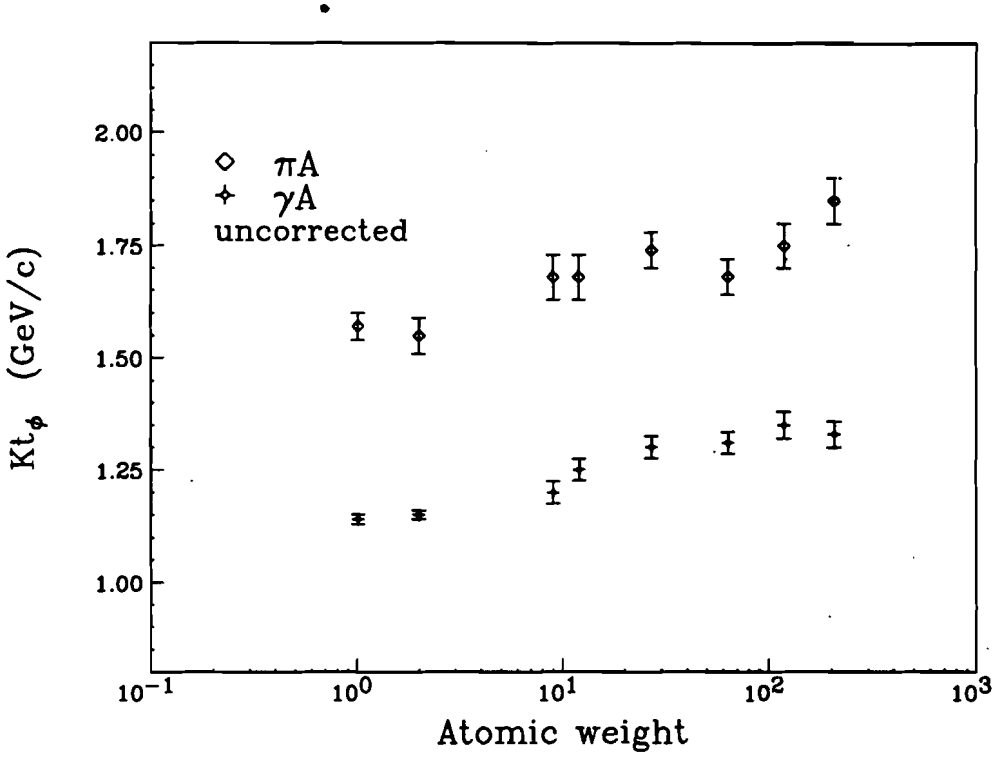


**Figure 30: A-dependence of $K_{t\phi}$ for $\pi A$ and $\gamma A$ collisions (uncorrected)**

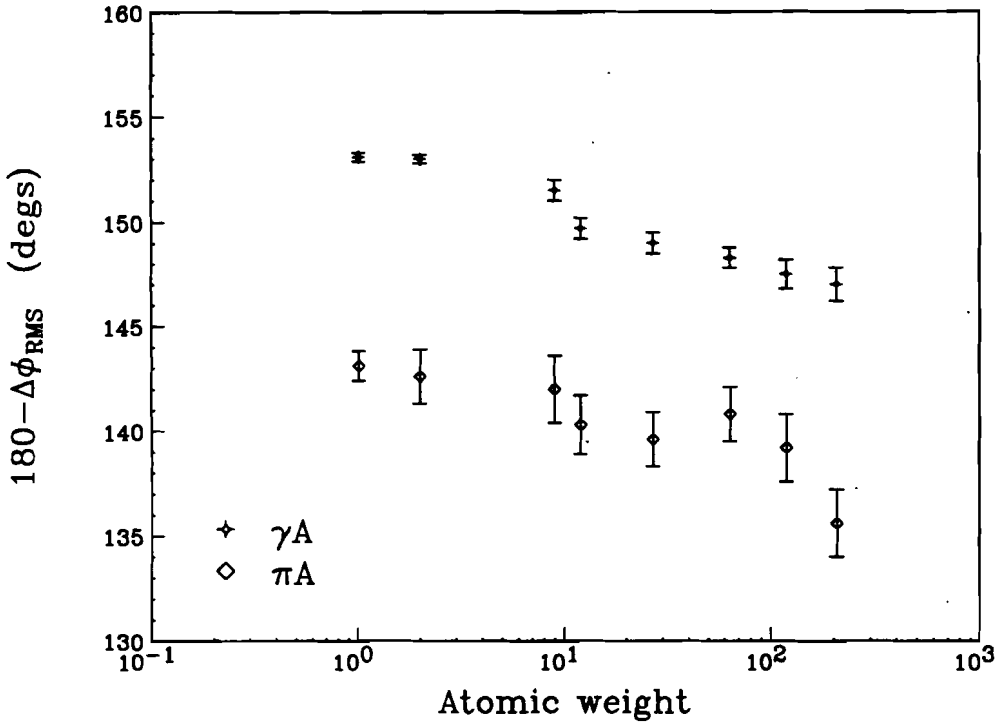


**Figure 31: A-dependence of $\Delta\phi$ for $\pi A$ and $\gamma A$**

malize the distributions was obtained by rescaling the measured trigger rates to account for the computer and trigger dead times. (The dead time is the time during which the computer or trigger circuit are busy processing a trigger event and are not available to accept new events which occur during the processing time). The empty target vessel runs were used as the empty target distribution for the $LH_2$ and the $LD_2$ targets and the 'blank' position on the nuclear target wheel was used to correct the nuclear targets.

The effect of the empty target subtraction on $K_{t\phi}$ for each target is shown in figure 32a for photon-nucleus data and 32b for pion-nucleus data. The uncorrected points are shown as crosses and the corrected points are the diamonds. The A-dependence increases slightly after the empty target subtraction is performed. The approximate value of $K_{t\phi}$ for the empty target is shown as a dashed line intersecting the curve. Both the cryogenic target vessel and the 'blank' position on the nuclear target wheel had approximately the same $K_{t\phi}$ .

The $K_{t\phi}$ of both empty target distributions are consistent with the events coming from a nucleus with effective atomic weight, $A_E \sim 10 - 20$. Carbon, oxygen and nitrogen are constituents of the non-target related event material (scintillators and target tent material) which fall approximately in the correct atomic weight range for candidates. The subtraction has the effect of increasing $K_{t\phi}$ for the targets with $A > A_E$ and decreasing $K_{t\phi}$ for targets with $A < A_E$.

The corrected data with error bars which reflect the convolution with the empty target errors bars is plotted in figure 33.

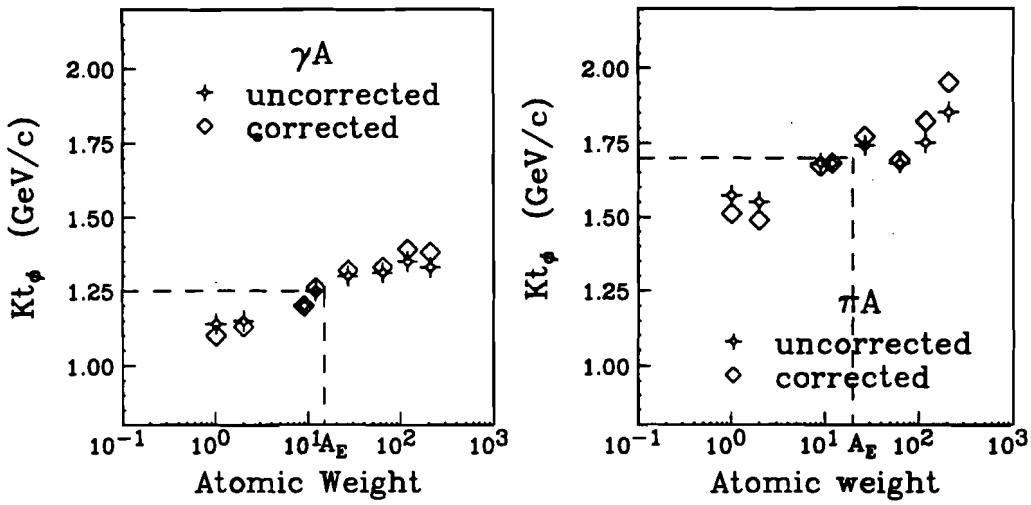


Figure 32: Effect of empty target correction on A-dependence a.) $\gamma A$ b.) $\pi A$ (the dashed line shows the approximate $K_{t\phi}$ value for the empty target distribution and its effective Atomic weight, $A_E$).

The slopes of the $\pi A$ and $\gamma A$ A-dependence look quite similar on this plot. However this representation is misleading. The large offset between the curves was explained as due to larger contributions from particle inclusion errors in jetfinding for pion interactions. Because the pion curve is sitting on a larger background that contributes in quadrature to $K_{t\phi}$ it actually has a stronger A-dependence behavior than $\gamma A$ . The nuclear contribution to $K_{t\phi}$ , $K_{t\phi NUCLEAR}$, is obtained by removing the value of $K_{t\phi}$ measured for the Hydrogen target from that for each target in quadrature. This assumes that nuclear contributions and those for the

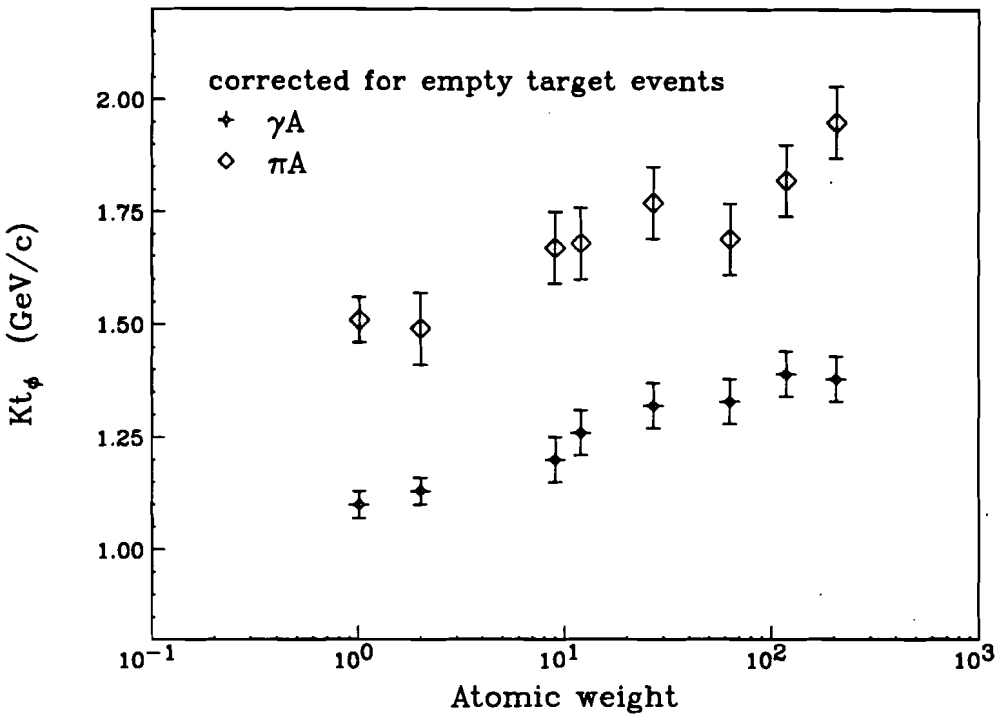


**Figure 33: A-dependence of $K_{t\phi}$ after empty target correction. (error bars reflect the convolution with the empty target's error bars).**

single nucleon are independent and are therefore uncorrelated. This assumption will be, at least partially, verified later. Figure 34 shows the nuclear contributions to $K_{t\phi}$ alone.

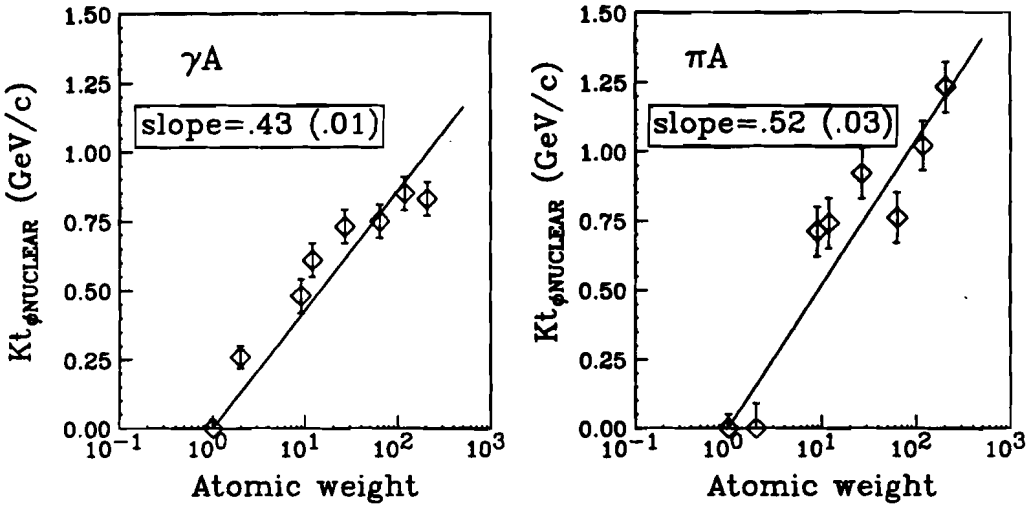


Figure 34: Nuclear contribution to $K_{t\phi}$ , $K_{t\phi NUCLEAR}$, as a function of Atomic weight.

We interpret this nuclear dependence of $\Delta\phi$ and $K_{t\phi}$ to be a result of a large perturbation to the parton direction such as could be caused by a hard rescatter or gluon radiation enhancement. As discussed in the first chapter these mechanisms lead to a broadening of the $\Delta\phi$ distribution with A. As the parton traverses more nuclear matter its probability for sucessive interacts with the medium is larger.

Linear fits were performed to both data sets so a comparison of the A-dependence can be made. There is no other motivation for this particular parameterization. The linear fits have slopes $0.43 \pm .01$ GeV for $\gamma A$ and $.52 \pm .03$ GeV for $\pi A$ . In

the linear paramaterization the $\gamma A$ and $\pi A$ slopes are comparable. The slope of the $\pi A$ curve is slightly larger. The difference appears to be significant at the level of the error bars of the fit.

The measurements of the A-dependence of $K_{t\phi}$ will be presented in one final form. This is done so that a physically reproducable quantity is presented that can then be compared with results from other experiments. Thus we must remove the contributions to $K_{t\phi}$ due to jetfinding errors and our detector that were discussed at the end of chapter 4. The jetfinding correction to $K_{t\phi}$ for photon beam data was found to be $0.6 \pm 0.1$ GeV using the LUCIFER/TWISTER Monte Carlo code that was a good model of our photon data. For the pion beam data it was more difficult to make the correction.

The LUND Monte Carlo codes did not reproduce our pion data due to their inadequate modeling of the soft underlying event collision that should be present in hadron-hadron collision. To see the effect of this contribution on our jetfinding errors an attempt was made to put this contribution into the LUND Monte Carlo code by hand. (You may recall that independent fragmentation option is needed to be able to define a 'true' jet of particles so that we cannot make this correction in the same way using HERWIG Monte Carlo).

This was accomplished by extracting the underlying event parameterization that was used in the HERWIG Monte Carlo. This enhanced underlying event

then replaced the underlying event in the TWISTER (which was tuned up to have the same hard scatter parameters as in HERWIG). The new hybrid Monte Carlo results compared well with those from HERWIG and with the pion data. The jetfinding contribution to $K_{t\phi}$ for pion beam data was found to be $1.3 \pm 0.2$ GeV using the hybrid Monte Carlo. This is about twice the size as correction for the photon data.

Figure 35 shows the data points with the respective jetfinding contributions subtracted in quadrature. These are the measured values of $K_{t\phi}$ for each target with contributions from the measurement removed. Our measured value of $K_{t\phi}$ for the Hydrogen target using the photon beam is 0.92 GeV with an estimated 0.1 GeV systematic error bar which comes from uncertainty in the jetfinding contribution. The value of $K_{t\phi}$ measured for the Hydrogen target using the pion beam is $0.77 \pm 0.2$ GeV. We will convert our measurement to the single component RMS using the relation defined above.

$$k_{tRMS}(\gamma p) = 1.15 \pm .14$$

$$k_{tRMS}(\pi p) = .96 \pm .25$$

Previous measurements with di-jets and Drell Yan at similar center of mass energies give results of between .8 and 1.1 [48] [49] [21]. Our values are comparable within the systematic error bars quoted.

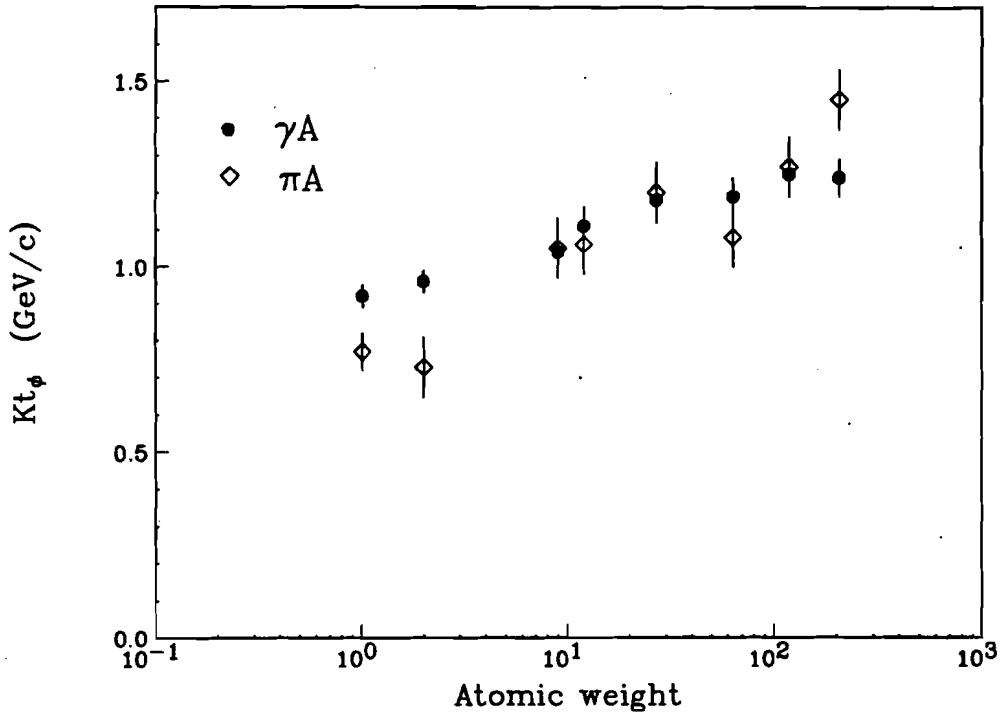


Figure 35: $K_{t\phi}$ measured for each target with the jetfinding contribution removed.

In subtracting the same value for jetfinding correction from each nuclear target it was implicitly assumed that the jetfinding contributions are not themselves a function of A. To show that this is indeed a reasonable assumption we have plotted the non-jet $E_t$ fraction as a function of A in figure 36. The non-jet $E_t$ fraction is the ratio of the $E_t$ outside of the jet cone divided by the total $E_t$ in the MCAL. It is the relative size of the hard scatter to the non-jet background which determines size of the jetfinding errors. That is, higher $P_t$ jets will be less affected by the background $E_t$ than those with a comparable amount of $E_t$ in both the hard scatter and the background. Thus the ratio should be a sensitive measure of the relative jetfinding contribution. The flat dependence of the non-jet $E_t$ fraction with A verifies that an A-dependent jetfinding correction is not needed.

## 5.3 Energy Dependence

Because of the unique broad energy beam spectrum used in this experiment we can look at the behavior of the A-dependence with energy. Ultimately, understanding of the energy dependence can lead to a better understanding of the mechanism for the A-dependence. No previous measurements exist for this and the systematic uncertainties in comparing results from two different experiments are large.

The photon energy was binned into four bins for the study; 150-200 GeV, 200-250 GeV, 250-300 GeV, and 300-350 GeV. The targets were then grouped into

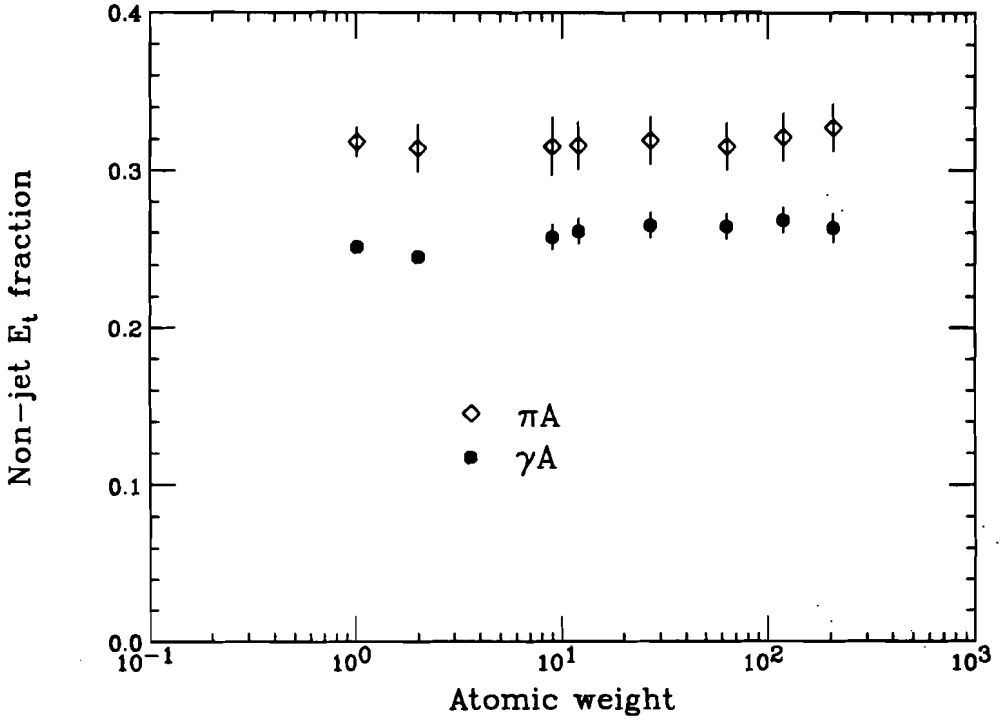


**Figure 36: Non-jet $E_t$ fraction for each target.**

three catagories; light, medium, and heavy in order to improve statistics. The light target consisted of Hydrogen alone. The Medium targets were Be, C, Al, and Cu which were given an effective atomic weight by weighting each target by the number of events it contributed, $A = 27.9$. The heavy targets were Sn and Pb with effective atomic weight, $A = 163$. $K_{t\phi}$ vs atomic weight is plotted in figure 37 for each energy bin.

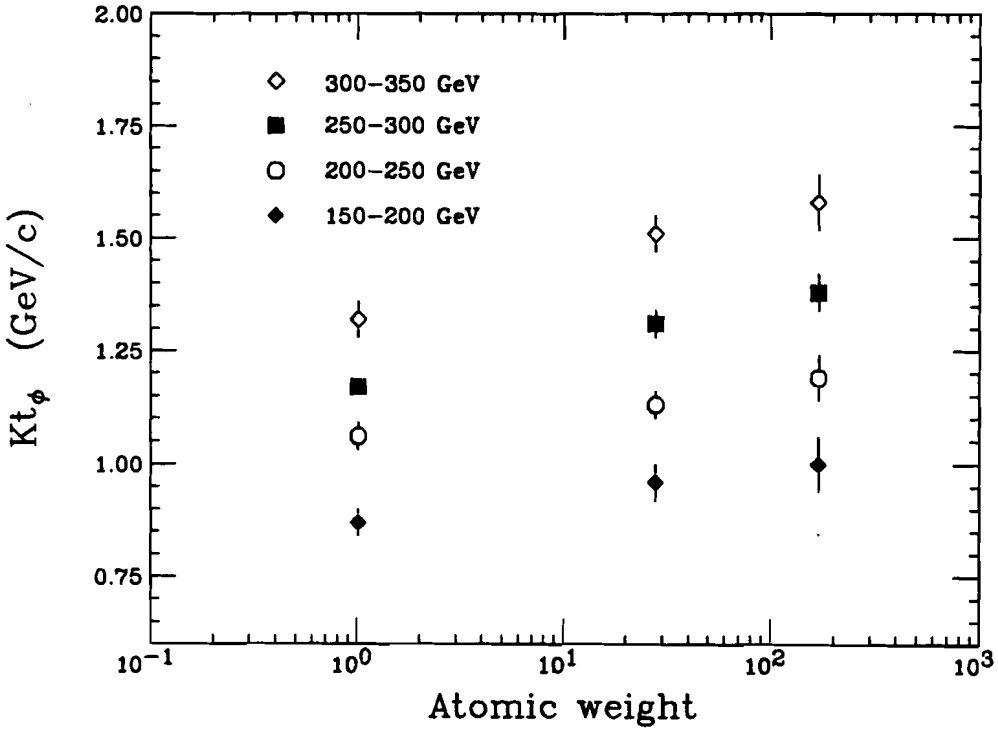


Figure 37: A-dependence of $K_{t\phi}$ at different beam energies.

As can be seen from the figure, the points not only appear to increase in slope with energy but the offset of the curves increases as well. The offsets of the

| *Energy* bin (GeV) | Mean Energy (GeV) | Fitted offset (GeV/c) |
|---|---|---|
| 150-200 | 166 | .87±.03 |
| 200-250 | 226 | 1.06±.03 |
| 250-300 | 274 | 1.17±.02 |
| 300-350 | 325 | 1.33±.04 |

Table 5.1: Fitted offsets of Energy dependence curves.

best fit lines at each energy are shown in table 5.1. One might expect an energy dependence in the offset to come about from the gluon radiation contributions to $K_{t\phi}$ . It can be argued that gluon radiation contributions would increase with energy due to the increased phase space for parton showering. However, $K_{t\phi}$ is also sensitive to underlying event contributions, which also could increase with energy. (Note that we do see an increase in the non-jet $E_t$ fraction with energy). Because the latter contribution is difficult to determine it is hard to say which is the dominating effect.

The nuclear dependence can be extracted by removing the hydrogen point at each energy in quadrature from each target. We have already seen that the underlying event, what ever its effect on the non-nuclear contributions, does not have an A-dependence. The nuclear contribution for each energy bin is shown in figure 38. The slopes of the curves appear to increase with energy. The curves show a saturation at high A. The curves are clearly not linear but we can use the slope of the linear fits to each curve for comparison. The fitted slopes are plotted

as a function of the mean $\sqrt{s}$ per bin in figure 39. This shows an increase with $\sqrt{s}$ in the slope.

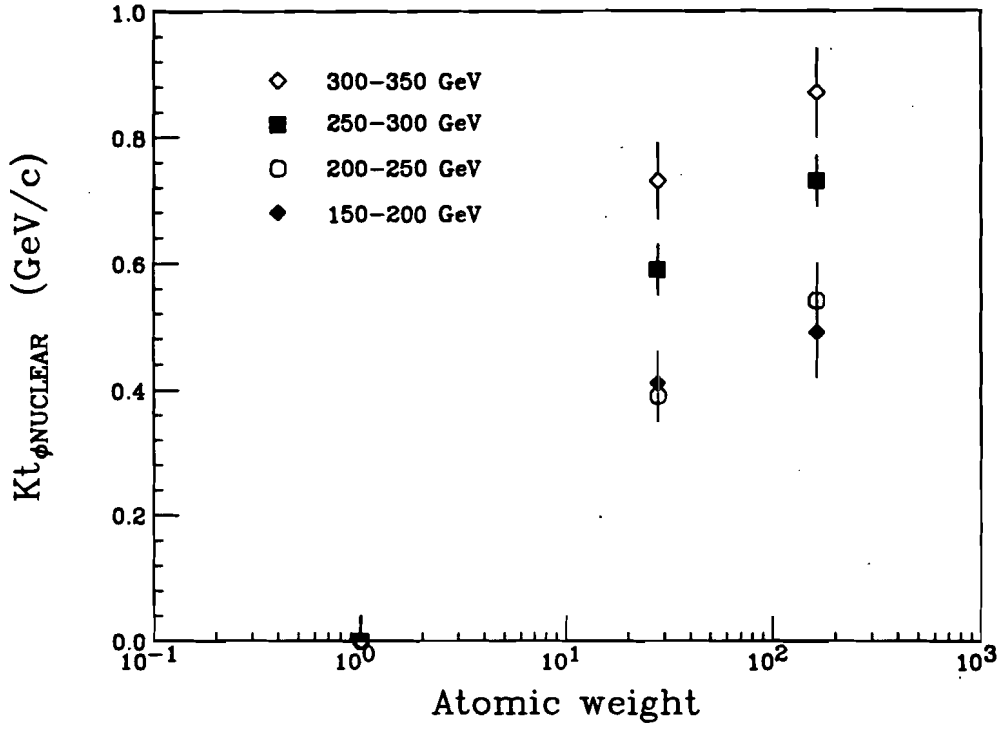


Figure 38: Nuclear contribution to $K_{t\phi}$ for each range of beam energies.

No empty target correction was made here due to lack of adequate statistics in each energy bin. We assume the effect of the target empty will not be energy dependent and will effect each of the curves by the same amount. The result will be to increase the slope of the energy dependence by a small amount.

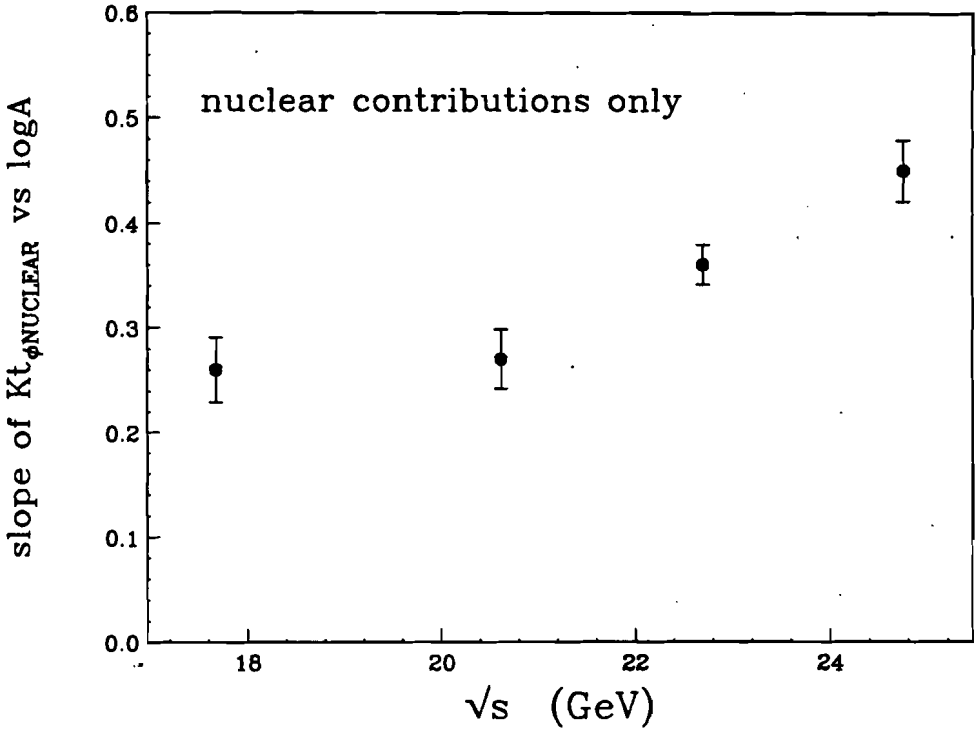


**Figure 39: Energy dependence of $k_{t\phi NUCLEAR}$ vs A.**

## 5.4 A-Dependence in Other Variables

Shown in figure 40 is the A-dependence of forward energy flow seen at three different depths in the BCAL detector. The same requirements of jet $P_t$ greater than 3 GeV and fiducial volume containment are imposed on the di-jet sample in this study as throughout the chapter. TOTAL is all the energy in the BCAL; L234 are layers 2, 3, and 4 (excluding layer 1); and L34 are just the deepest two layers. For the purpose of comparison an attempt was made to closely match the mean tag energy for the pion and photon data. This was accomplished by making a tag cut on the low end of the photon energy spectrum so that the two tag distributions had the same mean on average. Both spectra had a mean of about 275 GeV for the Hydrogen target. (The photon mean tag energy increased slightly with A, from 275 to 280 GeV). In addition, the 'NO pile up' cut was imposed on the photon data. This required that no electron be present in four buckets on either side of the beam bucket. The pion data was taken at a very low rate and did not have beam pileup.

For each depth the forward energy flow shown in $\gamma A$ appears to have little or no A-dependence, in contrast to $\pi A$ which has about 25% reduction from H to Pb in total energy. The 'TOTAL' BCAL energy for the photon data is greater than that for pion data while each of the other two layers is less than for the pion beam. This is an artifact of the beamline. That is, in section 2.4 it was estimated

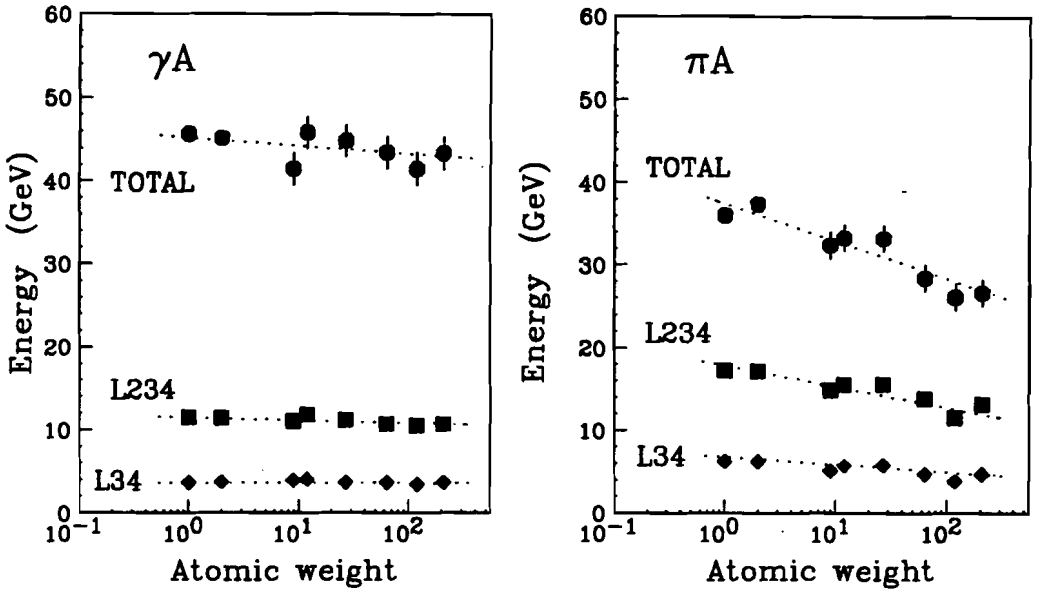


Figure 40: A-dependence of forward energy flow seen at three different depths in the BCAL detector. TOTAL is all the energy in the BCAL; L234 are layers 2, 3, and 4 (excluding layer 1); and L34 are just the deepest two layers.

from a GEANT simulation of the beamline that the mean soft forward energy flow due to multiple bremsstrahlungwith a 20% radiator is about 12 GeV. These soft photons cannot penetrate to the deeper layers of the BCAL. They will be stopped in layer 1. Thus the 'TOTAL' BCAL energy includes this contribution while the deeper layers do not.

To see where the lost energy is going (in the case of the pion data) we look at the mean MCAL energy as a function of A. This is shown in figure 41 for $\gamma A$ and $\pi A$ . It appears that the MCAL energy does not vary with A for both pion and photon data. Also plotted there are the mean BCAL energy and the

mean 'missing' energy obtained by the subtraction:

$$< EMISSING > = < EBEAM > - < EMCAL > - < EBCAL > .$$

The 'missing' energy in the event is the energy that was deposited outside of our detector acceptance. Some energy could also be missed by punch through of particles in the calorimeters or deposition in calorimeter dead spaces and cracks in the calorimeter.

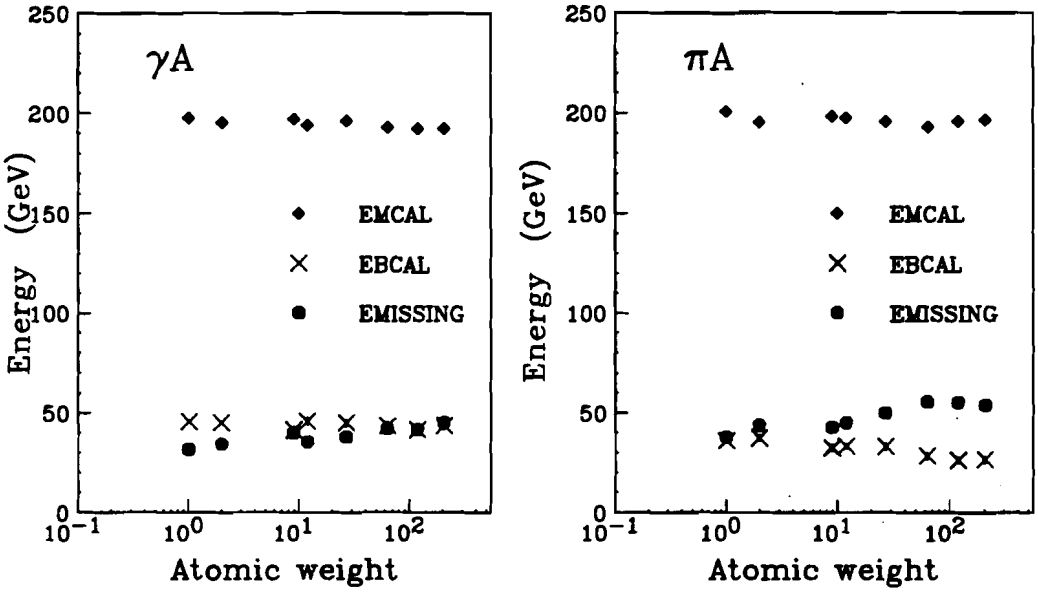


Figure 41: A-dependence of energy flow into the MCAL, BCAL, and target region.

The results for the energy flow in the pion data are in agreement with the results of E609 which found a very similar situation studying longitudinal energy flow for 400 GeV protons on nuclear targets [50]. In their case the forward energy

was reduced by about 40% in events from a lead target as compared with those from Hydrogen. Also, they found that very little of the missing energy was in the MCAL. They inferred that the 'missing' energy was flowing into the backward angular region ($\theta^* > 120°$ - the target region).

Reference [50] points out that one model which can explain the large decrease in forward energy flow in the case of $pA$ is that due to Daté, Gyulassy, and Sumiyoshi [51]. In this model the attenuation of the forward energy is due to the nuclear stopping power of the nucleus on the beam projectile. The nucleus is described as,"a parton filter sifting out a certian number of partons from the projectile." They formulate a model based on interactions of the color strings which connect interacting and spectator partons from the target and beam projectile. These color strings then interact with the nuclear medium as they are 'dragged' through it.

The above model can also explain the longitudinal energy flow seen in our pion data. It is not suprising that the longitudinal energy flow in $\gamma A$ does not have the same feature. We have already seen evidence for a difference in event topology in $\gamma p$ hard scatter events as compared with $\pi p$ indicating the absence of a beam jet in the former case. In the context of the Daté, Gyulassy, and Sumiyoshi model there are no extra partons in the projectile for the nucleus to interact with in the direct coupling case. Thus the additional color string connections that were

responsible for the energy dissipation are also not present.

One final variable that exhibits an A-dependence is the event planarity. This variable is not as discriminating as $K_{t\phi}$ and more difficult to make predictions for. The effects of non-jet $E_t$ and non-coplanarity are more difficult to decouple in this variable. In addition, it is sensitive to jet collimation. Thus the A-dependence is harder to interpret than the case of the variable $K_{t\phi}$ . The A-dependence is shown in figure 42.

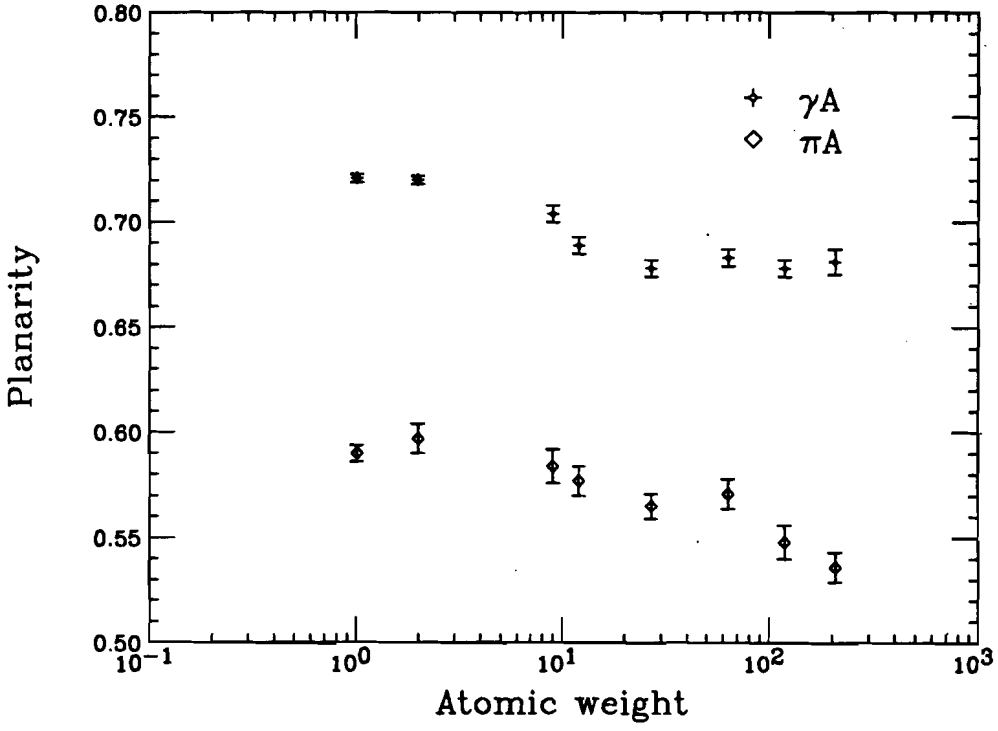


**Figure 42: A-dependence of event planarity for jet events.**

## 5.5 Conclusions

In this thesis we have studied jet events from photon-nucleus and pion-nucleus collisions. Jets from pion-proton collisions were seen to have substantially different $E_t$ flow that those from photon-proton collisions. In the $\pi p$ case the non-jet $E_t$ was a larger fraction of the total event $E_t$. $K_{t\phi}$ and $\Delta\phi$ were found to be much larger in $\pi p$ than in $\gamma p$ collisions.

The differences seen in $\pi p$ and $\gamma p$ jet events were studied in the context of a Monte Carlo comparison. Our $\pi p$ data was well reproduced by HERWIG Monte Carlo which includes a parameterization of the underlying event that is based on minimum bias $pp$ collision data. The photon data was modeled adequately by a combination of the LUND Monte Carlos, LUCIFER and TWISTER. We argued that the enhanced underlying event $E_t$ needed to explain our pion-proton data could be understood from the difference in event topology expected in $\pi p$ as compared with $\gamma p$ collisions.

We found that the jetfinding was affected by the underlying event $E_t$ present which accompanied the hard scatter event. The non-jet $E_t$ under the jet cone artificially boosted the true jet $P_t$ and smeared the angular determinations. A larger jetfinding contribution was present in the value of $K_{t\phi}$ measured from pion-produced jets than in photoproduced jets. After the jetfinding contributions were removed, the value of $K_{t\phi}$ measured from pion-proton data agreed reasonably with

that measured from photon-proton data and with previous measurements.

Both photon-nucleus and pion-nucleus collisions showed a strong A-dependence in the variables $K_{t\phi}$ and $\Delta\phi$. We interpret this A-dependence as a direct measure of nuclear rescattering of the interacting partons. The soft underlying event was independent of atomic weight. Thus the A-dependence seen in the hard scatter system was not contaminated by interference in the measurement from an A-dependent soft underlying event $E_t$. This supports the interpretation of rescattering in the hard scatter system.

The nuclear contributions to $K_{t\phi}$ measured for $\pi A$ appeared to be slightly larger than for $\gamma A$ . This trend seems to agree with results from a previous hadroproduction experiment, E609, which studied proton nucleus collisions at $\sqrt{s}$ of 28 GeV [21]. (Firm conclusions can not be made about the agreement because the experiments were preformed at a different $\sqrt{s}$). A weaker dependence of $K_{t\phi}$ with atomic weight in $\gamma A$ collisions may be explained by the absence of initial state incident photon interactions in the direct coupling photon case. There may be final state differences which could contribute as well.

The nuclear contributions to $K_{t\phi}$ for $\gamma A$ were found to increase with $\sqrt{s}$. This dependence might naively be expected from the $Q^2$ dependence of the gluon radiation contributions. The enhancement to the gluon radiation due to interaction with the nuclear medium might also be expected to increase with $\sqrt{s}$. Higher order

QCD calculations may be needed to understand this behavior [17]. A quantitative understanding of this energy dependence can lead to a better understanding of the mechanism for the A-dependence.

Longitudinal energy flow in $\gamma A$ and $\pi A$ also behave differently. There is very little decrease in the forward energy flow in $\gamma A$ with atomic weight whereas $\pi A$ has a substantial decrease ($\sim$ 25%) with atomic weight. Both beam types see little or no change in the energy deposited at wide angles (in the MCAL) with atomic weight. Daté et al [51] showed that the nucleus could have a large effect on the spectator partons in $pA$ collisions. A similar case can be argued for $\pi A$ collisions. In the case of $\gamma A$ collisions the flat behavior of longitudinal energy flow with A can be interpreted (in this context) as evidence for the absence of projectile spectator partons in the photon beam.

# Appendix

## Definition of Symbols

| | |
|---|---|
| $\phi$ | azimuthal angle (see figure 16) |
| $\theta$ | polar angle in the lab frame (see figure 16) |
| $\theta^*$ | polar angle in the $\gamma p$ center of mass frame |
| $E_t$ or $P_t$ | transverse energy $= E \sin\theta$ |
| $y$ | rapidity $= \frac{1}{2}\ln(\frac{E+p_z}{E-p_z})$ |
| $\eta$ | pseudorapidity $= -\ln[\tan\frac{\theta}{2}]$ |
| $\Delta\phi$ | azimuthal opening angle between di-jets |
| $K_{t\phi}$ | out-of-plane component of transverse momentum $=< P_t > \sin(\Delta\phi)$ |
| $k_{tRMS}$ | RMS value of $K_{t\phi}$ (given by $\sqrt{\frac{\pi}{2}}K_{t\phi}$) |
| $x$ | Bjorken $x$, fraction of four momentum carried by an interacting parton |
| $\sqrt{s}$ | total center of mass energy of the reaction |
| $Q^2$ | invariant four momentum transfer squared ($\propto P_t^2$) |

# Bibliography


[1] M. Breidenbach et al., *Phys. Rev. Lett.* **23** (1969) 935.

[2] M. Gell-Mann, *Phys. Lett.* **8** (1964) 214.

[3] F.W. Busser et al., *Phys. Lett.* **46B** (1973) 471.

[4] R. Feynman, R. Field, and G. Fox, *Phys. Rev. D* **18**, (1978) 3320.

[5] I. Park et al., *Phys. Rev. Lett.* **62** (1989) 1713.

[6] H. Fritzch, *preprint MPI-Ph/92-93* October 1992.

[7] NA14 collaboration, *Phys. Lett.* **168B** (1986) 163.

[8] OMEGA collaboration, *Z. Phys. C* **46** (1990) 35.

[9] M. Drees and R. Godbole, *Phys. Rev. Lett.* **61** (1988) 682; H. Baer, J. Ohnemus, and J. Owens, *Z. Phys.* **C42** (1988) 657.

[10] J.F. Owens , *Phys. Rev.* **D21** (1980) 54.

[11] R. Feynman and R. Field, *Nucl. Phys.* **B136** (1978) 1.

[12] T. Sjostrand, *Int. J. Mod Phys.* **A3**(1988) 751 (and references therein).

[13] Marchesini and Webber, *Nucl. Phys.* **B310** (1988) 461.

[14] G. Altarelli and G. Parisi, *Nucl. Phys.* **B126** (1977) 298.

[15] C. Bromberg at al., *Nucl. Phys.* **B171** (1980) 38.

[16] J. Morfin, Proceedings of the XXI Intl. Symp. on Multiparticle Dynamics Wuhan,China September 1991.

[17] M. Luo, J. Qui, and G. Sterman, *Phys. Lett.* **B279** (1992) 377.

[18] J. Cronin et al., *Phys. Rev. Lett.* **31** (1973) 1426.

[19] C. Bromberg et al., *Phys. Rev. Lett.* **42** (1979) 1202.

[20] Brown et al., *Phys. Rev. Lett.* **50** (1983) 11; Stewart et al., *Phys. Rev.* **D42** (1990) 1385.

[21] M. Corcoran et al., *Phys. Lett.* **B259** (1991) 209.

[22] T. Fields and M. Corcoran, *Phys. Rev. Lett.* **70** (1993) 143.

[23] D. Kaplan et al., *Phys. Rev. Lett.* **40** (1978) 435; P. Boraldo et al., *Phys. Lett.* **B193** (1987) 373; D. Alde et al., *Phys. Rev. Lett.* **64** (1990) 2479.

[24] G. Bodwin et al., *Phys. Rev. Lett.* **81** (1981) 1799; G. Bodwin et al., *Phys. Rev.* **D39** (1989) 3287.

[25] M. Lev and B. Petersson, *Z. Phys* **C21** (1983) 155.

[26] P. Chiappetta and H. Pirner, *Nucl. Phys.* **B291** (1987) 765.

[27] K. Kastella et al., *Phys. Rev.* **D39** (1989) 2586.

[28] T. Fields, *Nucl. Phys* **A544** (1992) 565.

[29] P. Frabetti et al., *Fermilab preprint 92/320-E*

[30] G. Alimonti et al., *NIM* **A314** (1992) 411.

[31] K. Johns, *Rice Univ. MA Thesis*, unpublished (1983); M. Arenton et al., *Phys. Rev.* **D31** (1985) 984; W. Selove et al., *NIM* **161** (1979) 233.

[32] D. Naples, *internal note "Summary of Progress in Understanding the RESH - BCAL system"*, July 92.

[33] D. Lincoln, *internal note*, October 1992

[34] D. Lincoln, *Rice Univ. MA Thesis*, unpublished, (1990).

[35] D. Lincoln, *internal note "BCAL Response Summary"*, June 1992.

[36] D. Lincoln and D. Naples, *Univ of Maryland preprint PP#93-098* (submitted to NIM December 1992).

[37] R.Brun et al., *CERN-DD/EE/84-1* **GEANT** September 1987, 175pp.

[38] M. Corcoran, *internal note* "Summary of anti- muon cuts".

[39] B. Flaugher and K. Meier, *preprint FNAL-90/248-E*, December 1990

[40] T. Sjostrand, *Comp. Phys. Comm.* **39** (1986) 347; Bengtsson and Sjostrand, *Comp. Phys. Comm.* **46** (1987) 43.

[41] Marchesini and Webber, *Comp. Phys. Comm.* **67** (1992) 465.

[42] G. Ingelman and A. Weigand, *Comp. Phys. Comm.* **46** (1987) 241.

[43] G. Ingelman and A. Weigand, *Comp. Phys. Comm.* **46** (1987) 217; T. Sjostrand, *Comp. Phys. Comm.* **43** (1987) 367.

[44] M. Corcoran, *internal note* "E683 MCAL simulator update".

[45] Marchesini and Webber, *Phys. Rev.* **D38** (1988) 3419.

[46] G. Alner et al., *Nucl. Phys.* **B291** (1987) 45.

[47] T. Sjostrand, *CERN-TH.6488/92* PYTHIA Physics Manual (p.183-192).

[48] M. Corcoran et al., *Phys. Rev.* **D21** (1980) 641.

[49] D. Kaplan, *Phys. Rev. Lett.* **40** (1978) 435.

[50] C. Moore et al., *Phys. Lett.* **B244** (1990) 347.

[51] S. Daté, M. Guylassy, and H. Sumiyoshi , *Phys. Rev.* **D32** (1985) 619.